Object-based continuous monitoring of land disturbances from dense Landsat time series

3 authors:

Su Ye
Zhejiang University
20 PUBLICATIONS   441 CITATIONS

SEE PROFILE

Zhe Zhu
University of Connecticut
85 PUBLICATIONS   12,807 CITATIONS

SEE PROFILE

Guofeng Cao
University of Colorado Boulder
69 PUBLICATIONS   1,871 CITATIONS

SEE PROFILE

Some of the authors of this publication are also working on these related projects:

Project   Mapping and Characterizing Human Activity Changes using NASA Black Marble Product Suite   View project

Project   Geostatistics of heterogeneous spatiotemporal data   View project

Contents lists available at ScienceDirect

Remote Sensing of Environment

Object-based continuous monitoring of land disturbances from dense Landsat time series

Su Ye [a,*], Zhe Zhu [a], Guofeng Cao [b]

[a] *Department of Natural Resources and the Environment, University of Connecticut, Storrs, CT, USA*
[b] *Department of Geography, University of Colorado Boulder, Boulder, CO, USA*

ARTICLE INFO

ABSTRACT

An accurate mapping of land disturbances with regard to their timing and locations is the prerequisite for the success of downstream disturbance characterization. This study introduces and tests a novel approach that integrates a spatial perspective into the dense Landsat time series analysis, called "Object-Based COntinuous monitoring of Land Disturbance" (OB-COLD). The new algorithm is based on the recognition that the pixels under effects of the same disturbance event often present similar spectral change concurrently in a short time; such pixels experiencing concurrent change could be grouped as an analytic spatial unit, namely "change object". OB-COLD first generates a change-magnitude snapshot every 60 days by applying per-pixel time series analysis to measure spectral change history. Then, an object-based change analysis is applied for each time-stamped snapshot: two levels of change objects are generated through over-segmentation and region merging; the changing area is determined by examining three object-level properties derived at different scales: the average change magnitude, the pre-change cover type, and the object size. Lastly, OB-COLD reconstructs model coefficients for each temporal segment based on the temporal breaks indicated by new snapshot-based change maps. We tested the new algorithm using 3000 randomly selected reference sample plots and eight Landsat ARD tiles across the continental United States. The accuracy assessment suggests that OB-COLD achieved 76.9% producer's accuracy, which is significantly higher than the per-pixel time series algorithm (i.e., COLD) (16.3 percentage increase) while keeping a comparable user's accuracies (58.7% vs. 57.8%). The quantitative and qualitative evaluations both suggest that OB-COLD could significantly reduce omission errors, particularly for stress disturbances. Most commission errors (73%) are attributed to agricultural practices and climate variability. The proposed algorithm is computationally scalable to large-scale spatiotemporal datasets with advanced cyberinfrastructure resources, holding great potential as the base detection algorithm for the next generation of land disturbance products.

1. Introduction

Land disturbance, not limited to forested regions, can be defined as any event that is relatively discrete in time and space that disrupts the structure of an ecosystem, community, or population (Newman, 2019; White and Pickett, 1985). Land disturbances, purportedly driven by anthropogenic activities and recent climatic warming, have been documented over large parts of the globe with an increase in frequency and severity (Dale et al., 2001; Seidl et al., 2017), yielding significant impacts on the carbon cycle (Liang et al., 2014; Seidl et al., 2014), biodiversity (Martínez-Ramos et al., 2016), water quality (Carey et al., 2011) and landscape composition (Danneyrolles et al., 2019). Timely

and accurate mapping of land disturbance events is of enormous importance to ecologists and forest managers, allowing for a better understanding of ecosystem-climate interactions and improved land resource management (Cohen et al., 2016; Rogan and Miller, 2006; Senf et al., 2017; Senf and Seidl, 2021). Remote sensing technology, typically the medium-resolution time series analysis, has been widely used for detecting a variety of land disturbances by identifying a temporal span of spectral anomaly relative to its natural variability (Coops et al., 2020; Hermosilla et al., 2019; Schug et al., 2018; Villarreal et al., 2016; Yin et al., 2020; Zhu et al., 2019). A satellite-based disturbance investigation project is typically comprised of two components: 1) mapping of disturbed region and timing (Cohen et al., 2018; Huang et al., 2010; Zhu

et al., 2020); 2) characterizing disturbance agents (Baumann et al., 2014; Kennedy et al., 2015; Zhang et al., 2022), severity (Rodman et al., 2021), or recovery (White et al., 2022). This paper is concerned with the first component, the process of detecting disturbances, which provides essential base maps for downstream disturbance characterization.

To date, numerous algorithms have been developed to map disturbances from Landsat time-series dataset (Zhu, 2017). COntinuous monitoring of Land Disturbances (COLD), the latest version of the Continuous Change Detection and Classification (CCDC) algorithm tailored for land disturbance mapping, is a representative approach that makes it feasible to detect a variety of land disturbances based upon all available Landsats 4–8 data (herein named as "dense time series", Zhu et al., 2020). COLD or all CCDC-like algorithms successively compare model forecasts and actual observations and identifies breaks if the discrepancies between new observations and model predictions persist (Zhu et al., 2020; Zhu and Woodcock, 2014a), which have been widely used for mapping coastal tidal wetland dynamics (Yang et al., 2022), land disturbance agents (Qiu et al., 2022), nighttime light change (Li et al., 2022) and forest dynamics (Healey et al., 2018).

While COLD and other popular time-series approaches, such as LandTrendr (Kennedy et al., 2010), BFAST (Verbesselt et al., 2010), and VCT (Huang et al., 2010), have greatly enhanced our ability for mapping land change, these methods adhere to using pixels as independent spatial units for analysis, focusing on capturing obvious temporal anomaly or breaks based upon single-pixel-based time series. The major downside for such-like approaches is that they often suffer a high omission error rate for the myriad of subtle disturbances (e.g., insect, drought) that are characterized by insignificant spectral change lower than their pre-defined magnitude threshold (Cohen et al., 2017; Ye et al., 2021b; Zhu et al., 2019). Even for the dramatic disturbances that lead to land cover conversion (e.g., agricultural expansion and urbanization), per-pixel approaches may fail to delineate the full extent of a disturbance-affected region that often presents heterogeneous change owing to numerous geographically varying factors such as severity, pre-disturbance conditions, and topography. Spatial-contextual information, such as patch size and change adjacency, could provide new powerful metrics for discriminating subtle disturbances and enhance detection completeness through a consideration of spatial autocorrelation for event-induced spectral change. To incorporate spatial information into temporal analysis, several studies applied a simple spatial filtering for post-processing disturbance maps (Pasquarella et al., 2017; Ye et al., 2021b) but often only achieve a small degree of map refinement (Ye et al., 2021b). More sophisticated is a group of spatial-window techniques that uses a focal operation to preprocess each original satellite image and then applies the time-series algorithm to the preprocessed images (Hamunyela et al., 2016; Meng et al., 2021). For example, Hamunyela et al. (2016) normalized each pixel by the median value of the neighboring pixels whose vegetation index values are above the 90th percentile of all pixels within a spatial window; such spatial normalization could significantly reduce signal noises from vegetation phenology for the subsequent time series analysis and advance the timing of capturing deforestation signals (Hamunyela et al., 2016). This study was targeted at forest disturbance, and the window size was determined through sensitivity analysis (Hamunyela et al., 2016); however, a single predefined spatial window size may not be sufficient for modeling generic land disturbances at a national or continental scales, which often manifests a diversity of cover types, spatial patterns and extents.

Object-Based Image Analysis (OBIA) is an image processing framework which divides an image into clusters of adjacent pixels based on their spectral similarities, i.e., image objects (IOs), and then uses these IOs as the analytic unit (Blaschke, 2010) for the tasks such as image classification (Dronova et al., 2015; Gudex-Cross et al., 2017; Zhang et al., 2014, 2018), continuous surface parameter estimate (Laurent et al., 2013; Roelfsema et al., 2014), and pansharpening (Zhang et al., 2021). IOs can be used to represent an almost unlimited range of

phenomena (Bian, 2007), from meaningful landscape entities to a lower-level grouping of spectrally similar pixels such as superpixel (e.g., Csillik, 2017), thereby leading to more flexibilities for modeling complex geographic phenomenon than the spatial-window techniques. OBIA first gained its popularity among the fine-resolution (< 5 m) applications under an H-resolution situation (Cleve et al., 2008; Holt et al., 2009), where landscape units of interest are significantly larger than the resolution cells (Strahler et al., 1986). Later studies utilized OBIA for medium-resolution images such as Landsat (Duveiller et al., 2008; Jobin et al., 2008; Vieira et al., 2012) and Sentinel-2 (Belgiu and Csillik, 2018; Djerriri et al., 2020), owing to its superiority for incorporating spatial properties such as object size and texture. These OBIA studies were mainly employed for land cover classification tasks, defining their objects as landscape entities. Nevertheless, land disturbances not only alter landscape units in terms of their biophysical properties, but also – and more often – change their spatial borders. Therefore, it is unlikely to apply an object-oriented paradigm based on land cover objects for mapping land disturbances, unless targeted landscape boundaries remain unchanged during the change process (e.g., Yin et al., 2018).

Alternatively, we could choose change objects as our analytic unit, rather than land cover objects. The consequences of a disturbance event, such as altering land condition, composition, soil property, or cover types, are often viewed as a spatial and temporal continuum (Kimmins, 2004). If a pixel is experiencing spectral changes related to a disturbance, it is reasonable to expect that its neighboring pixels present similar spectral changes in a synchronized manner, constituting a change object. This definition resolves the issue of changing object boundaries over time and facilitates integration of object-level change features, such as change object size and pre-change land types, for improved disturbance detection.

Closing this gap, the change-object approach embarks on a similar challenge in GIScience concerning the representation of complex spatiotemporal objects across multiple spatiotemporal scales (Blaschke et al., 2014; Yuan, 2001). Particularly, enormous spectral details have been brought by within-event change heterogeneity, as well as increasing temporal density and spatial resolution of satellite images, calling for a hierarchical, multi-scale framework to decompose the spatiotemporal complexity. Fig. 1 conceptualizes a three-level hierarchy for perceiving a change process from a medium-resolution time-series dataset typically with a revisiting cycle of 3–8 days. Change superpixels (Level III) refer to a grouping of pixels that share common spectral change in a short interval (e.g., a month) under the effects of a process, representing the most detailed spatiotemporal object representation. The adjacent change superpixels within the same time intervals are further aggregated into a change patch (Level II), forming a continuous region affected by the change process at a coarser spatial scale. A change-process object (Level I) is the total area affected by the change process, which sometimes necessitates an ensemble of change information from several time periods (such as one to several years). Change-process object could be created by segmenting intermediate change measurement maps at an interval of multiple years (Gómez et al., 2011) or connecting adjacent pixels from annual pixel-based disturbance maps (Hermosilla et al., 2015; Kennedy et al., 2015; Qiu et al., 2022), and was commonly employed as the object unit for the disturbance characterization. On the contrary, change objects at a fine spatiotemporal scale are more practically useful at the detection stage which aims at delineating accurate spatial and temporal change boundaries, particularly to the CCDC-like approaches that were established to provide intra-annual change information. Besides, a fine temporal grain for monitoring can help reduce the chance of misidentifying a mixed-disturbance object and holds great promise for timely alerting in a near real-time monitoring task. To our best knowledge, there are no established approaches yet for analyzing change objects at a fine temporal scale (e.g., monthly). Specifically, two key impediments to such methodological development are: 1) lacking a way for extracting change objects from a time-series perspective of perceiving a spectral change relative to its historical
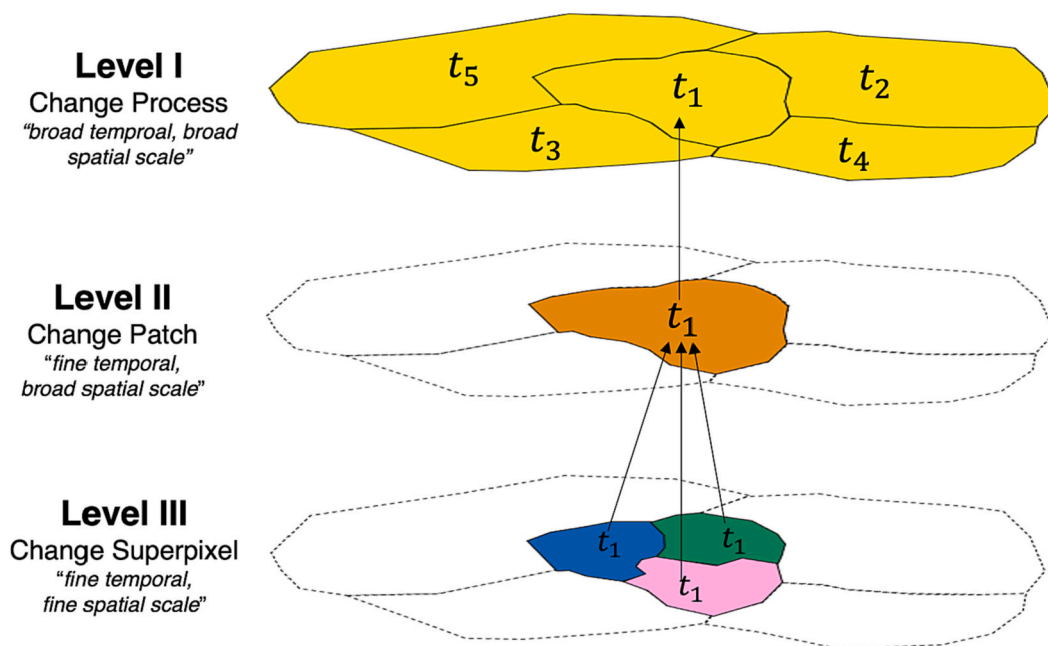
Fig. 1. A three-level hierachy of land-change objects from a spatiotemporal domain.

variation; 2) lacking a mechanism for intelligently integrating cross-scale information into the change-decision process.

In this study, we will describe a novel spatial-temporal algorithm for improved detection of land disturbances from Landsat time series dataset, called Object-based COntinuous monitoring of Land Disturbance (OB-COLD). The basic idea of OB-COLD is that we discretize continuous time into a series of equal time intervals as the analytical unit, i.e., time slices, allowing for a generation of image-like change snapshots at a fine temporal scale; then apply an OBIA procedure to delineate change regions within each snapshot by combining both change-superpixel and change-patch information. In what follows, we will introduce calibration and validation datasets (Section 2), provide technical details for OB-COLD (Section 3), present both quantitative and qualitative evaluation (Section 4), and finally discuss key issues in incorporating spatial and thematic information, validation, downstream disturbance characterization, etc. (Section 5).

2. Study area, datasets, and evaluation

2.1. Study area and datasets

Our algorithm tests were performed based on the CONUS (Conterminous United States) region. Two openly accessed CONUS-wide disturbance plot datasets, i.e., Cohen's dataset (Cohen et al., 2016) and LCMAP reference dataset (Pengra et al., 2020), were chosen as our reference dataset for model calibration and evaluation, which were used in multiple land change related studies (Cohen et al., 2016; Stehman et al., 2021; Ye et al., 2021a; Zhu et al., 2020).

In this study, detectable disturbances are defined as any discrete event that occurs beyond its natural variability of land surfaces on a decade scale; the spectral signals must be evident in both Landsat image chips or Landsat-based time series. Both subtle (e.g., stress) and dramatic disturbances (e.g., fire, harvest, and hydrology) are considered as our detection targets; on the contrary, climate variability and agricultural practice, which often induces ephemeral spectral fluctuation, are not counted within our detection scope. Based upon the Land Change Monitoring, Assessment and Projection (LCMAP) project and other past land disturbance studies (Pengra et al., 2020; Qiu et al., 2022; Zhu et al., 2020), the seven focused disturbance types in this paper were *fire, harvest, hydrology, mechanical, stress, debris,* and *other*. For a detailed

definition of these seven disturbance types, we refer the readers to Table 1 in Qiu et al. (2022).

Cohen's dataset (Cohen et al., 2016) was mainly used for model calibration in this study because this dataset adopted a forested-oriented sampling strategy (forest occupy 40% of the sample pool) and hence had less representativeness as a validation set for a generic land disturbance mapping. Cohen's dataset was generated from 180 Thiessen Scene Areas (TSAs, designed to provide non-overlapping Landsat-like frames for a convenient computation of unbiased estimator) polygons, which were sampled with a focus on the forested area from a total of 442 TSAs. Within each of the 180 TSAs, 40 Landsat plots were selected based on a simple random strategy, making up an initial sample set of 7200 Landsat plots. The disturbance years ranging from 1982 to 2012 were interpreted for each plot using a visualization software called TimeSync (Cohen et al., 2010). For more processing details, we refer readers to (Cohen et al., 2016; Zhu et al., 2020). A total of 6491 plots (blue dots in Fig. 2) remained after eliminating those sample plots that did not have enough clear sky observations (< 24) or were too difficult to interpret. Admittedly, Cohen's dataset was designed with a focus on the forested area, possibly causing the resultant model to yield more weights on

Table 1
A summary of land cover types and major disturbance agents for pilot sites.

Evaluation site/tiles	Dominant land cover types	Major disturbances
New England (h30v6)	Tree cover, developed, wetland	Gypsy moth outbreak, urban expansion, hurricane
Corn Belt Plains (h21v8)	Cropland, developed	Urban expansion, agricultural practice
Mississippi River Lowlands (h21v15)	Tree cover	Harvest, forest thinning
Western Great Plains (h14v6)	Grass, shrub, cropland	Drought
Rocky Colorado (h11v9)	Tree covers, cropland, grass, shrub	Beetle disturbances. agricultural practices
Cascades Plateau (h4v2)	Tree cover, grass, shrub	Logging, forest fire
West California (h2v8)	Cropland, grass, developed	Wildfires, agricultural practices
South Florida (h27v19)	Wetland (mangrove)	Tornado
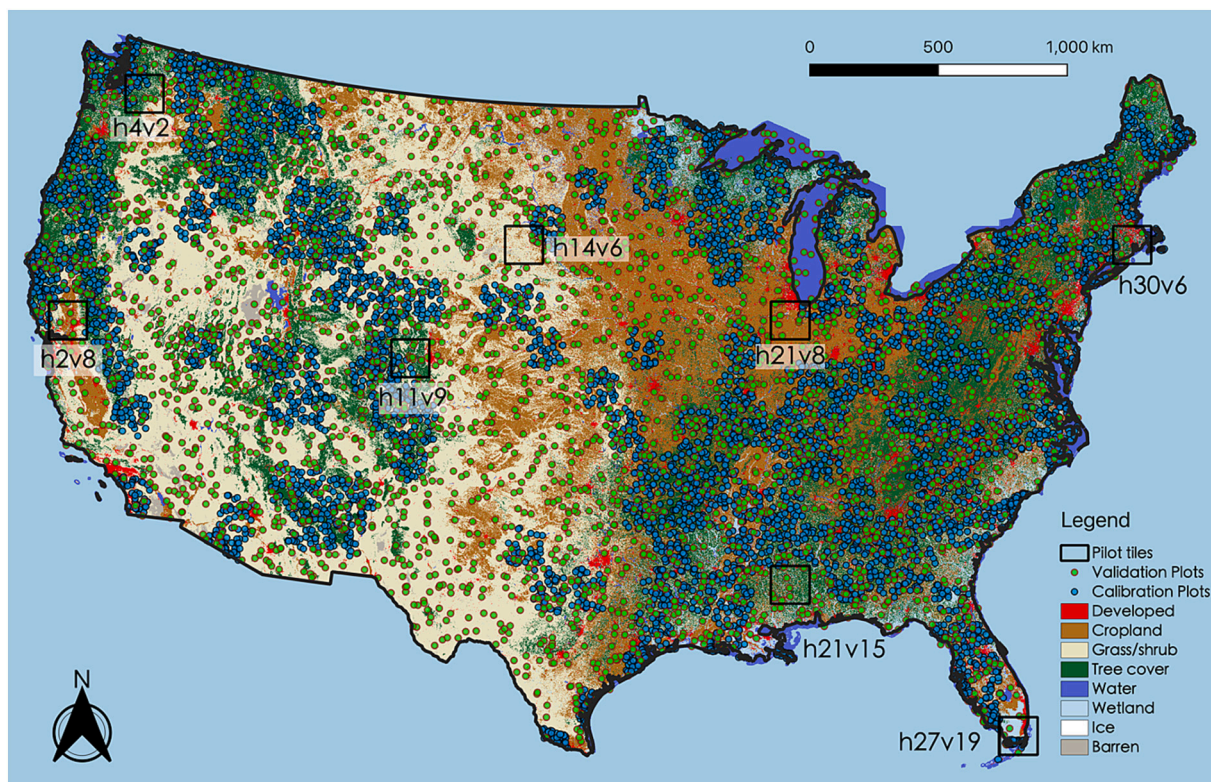
Fig. 2. Locations of 6491 calibration plots, 2880 validation plots, and pilot testing tiles. Cover map source: 2001 Land Change Monitoring, Assessment and Projection (LCMAP) primary land cover product (Version 1.2, Brown et al., 2019; Xian et al., 2022). (For interpretation of the references to color in this figure legend, the reader is referred to the web version of this article.)

forest disturbance detection. This problem could be alleviated by our cover-specific model establishment (see section 3.2.3): forest disturbance sample plots were only used to tune the stable model for three cover types with relatively small natural spectral variability (i.e., forest, water, and developed), which did not affect the model calibration for the other highly dynamic cover types (namely "fluctuated model"), such as cropland and grass.

Quantitative evaluation was conducted based on land change reference sample plots from the LCMAP project (Pengra et al., 2020), which were sampled from 30-m Landsat pixels in the CONUS ARD grid system. The LCMAP sample plots were generated from cluster-based sampling, in which each pixel was a cluster of 34 observation years of this pixel (Stehman et al., 2021). We chose LCMAP reference dataset rather than Cohen's dataset for validation as LCMAP reference dataset have no bias for specific land cover types, while Cohen's dataset was mainly located at forest-dominated TSAs. While LCMAP reference dataset was developed with a high quality following a rigorous protocol, we observed two primary issues causing its discrepancies with our detection scope: 1) disturbance omissions for ephemeral droughts that also induce a large-area spectral change from Landsat image chips as well as temporal break in the time-series profile (see the example of Fig. S1 in the supplementary), especially in semi-arid regions; 2) disturbance commissions caused by a spatial misalignment between the sample location and the disturbance extent (often at the edge of a large disturbance patch), where the sample pixels do not present an obvious change signal in the time series but misidentified as disturbances in the LCMAP reference set (see the example of Fig. S2 in the supplementary). Given these issues, we randomly selected 3000 sample plots from the 24,971 total sample plots and manually corrected sample plots from the convergence of visual evidence available in both temporal profiles and Landsat image chips, backed up by referencing historical high-resolution Google imagery. We excluded 120 sample plots (4.0%) that were extremely difficult to interpret due to too frequent spectral variation (mostly in semi-arid

regions, see the example Fig. S3). As a result, 2880 time-series sample plots were remained for the final model evaluation, resulting in a total of 97,920 validation cases for 34 years, which include 1230 disturbance years and 96,690 non-disturbance years. A total of three rounds of manual inspection were given to all validation cases, ensuring their correctness and consistency with the calibration dataset.

All Landsat ARD Collection 1 surface reflectance products between 1984 and 2021 (38 years) were downloaded for analysis. The Landsat ARD products gridded all available Landsats 4–8 as tiled, georegistered, and atmospherically corrected products defined in a common equal area projection (Dwyer et al., 2018). To facilitate model calibration and evaluation, we cropped a smaller time-series chip (53*53 pixels) for each reference plot. The width of 53 pixels was determined by covering 99% of patch-level change objects from running the default models for four pilot tiles.

2.2. Model calibration and evaluation

F_2 was chosen as the objective function for the model calibration. Combining the producer's accuracy (PA, a.k.a., recall) and the user's accuracy (UA, a.k.a., precision), a general form of F-score can be denoted as (Baeza-Yates and Ribeiro-Neto, 1999):

$$F_\beta = \left(1 + \beta^2\right) * \frac{UA * PA}{\beta^2 * UA + PA} \tag{1}$$

F_2 set $\beta = 2$ such that PA is considered twice as important as UA, motivated by that under-detection is more critical than over-detection for the ensuing disturbance analysis. There is almost no effective way for re-identifying a disturbance region if it is missed from the detection stage, while it is often methodologically possible to eliminate commissions through a spatial-contextual post processing such as sieving filter (Ye et al., 2021b) or through disturbance agent classification (Zhang et al., 2022). The calculation of UA and PA for the cluster sampling is the

same as that from the random sampling strategy (Stehman et al., 2021).

For model evaluation, we chose the performance metrics that were commonly used in previous disturbance detection studies (Galbraith et al., 2019; Solórzano and Gao, 2022; Ye et al., 2021a; Zhu et al., 2020) concerning communication, i.e., F_1 score, F_2 score, user's accuracy (UA) and producer's accuracies (PA). To our knowledge, COLD is the only algorithm targeted at medium-resolution generic land disturbance detection and hence will be used as the primary baseline for comparative analysis. The default COLD uses change probability $P = 0.99$ based on its best-balanced accuracy (i.e., F_1 score) (Zhu et al., 2020). To make it consistent with OB-COLD's calibration manner, we will also report the COLD performance with $P = 0.95$, which achieved the best F_2 score based on the same calibration dataset (see Table S1 in the supplementary).

In addition to quantitative evaluation, the qualitative assessment was performed for eight pilot Landsat ARD tiles (see the black hollow rectangle in Fig. 2), representing a broad range of ecoregions and disturbance agent types. Major land cover patterns and disturbance agents for these eight tiles were summarized in Table 1. The evaluation was accomplished by visually assessing OB-COLD disturbance maps in conjunction with the COLD disturbance maps and high-resolution Google Earth imagery (Section 4.2).

3. Method

OB-COLD consisted of three steps (Fig. 3). First, OB-COLD applies COLD to analyze per-pixel spectral change history and save change magnitudes at a regular temporal interval (i.e., time slice). Second, OB-COLD reorganizes these per-pixel change magnitudes into a sequence of image-like temporal snapshots and applies object-based change analysis to identify change regions for each snapshot. Finally, OB-COLD reproduces temporal segment characterization as change records based on the new spatially indicated breaks. It is worth mentioning that Steps 1 and 2 focus on the detection of general change processes including both land disturbances and other ecological processes such as natural recovery; land disturbance regions will be sorted out by applying a rule-based strategy in Step 3.

3.1. Temporal change measurement

OB-COLD adapts COLD (Zhu et al., 2020), a well-established algorithm for dense Landsat time-series, to analyze per-pixel spectral change history as its first step. Same to COLD, OB-COLD uses the Quality Assessment band generated by the Fmask algorithm (Zhu and Woodcock, 2012) to screen out the initial cloud, cloud shadow, and ice/snow, and then applies Tmask (Zhu and Woodcock, 2014b), a time-series-based outlier removal technique, to further remove remaining noises. The only modification is that OB-COLD generates two extra outputs from the COLD algorithm at a regular day interval, i.e., (1) the representative change magnitude and (2) its associate change date. For a time series $\{x_t, t \in T\}$ (T is the set of image acquisition dates), COLD identifies a spectral break if 1) an observation x_t has a change magnitude (CM_t), the minimum squared norm of standardized change vectors (CV) among a peek window (ψ) of k consecutive observations since a Julian date t, greater than a change threshold from the chi-square distribution at a probability of P (modified from Eq. 8 in (Zhu et al., 2020)):

$$CM_t = \min_{x \in \psi}\left\{\|CV_x\|^2\right\} \rangle \chi^2_P(5)$$ (2)

2) a mean included angle (β_t) between the ith and $(i+1)$th consecutive observations within the peek window is lower than $45°$ which excludes the noisy signals that have a large variation of change direction (Eq. 9 in (Zhu et al., 2020))

$$\beta_t = \frac{1}{k}\sum_{i=1}^{k-1}\beta_{i,i+1} < 45°$$ (2)

OB-COLD outputs a representative change magnitude for each time slice at a per-pixel level to indicate the overall change likelihood for the time slice, irrespective of break detection. Given a time slice $\varnothing$, its representative change magnitude ($CM_\varnothing$) combining the two decision intermediates, CM_t and β_t, is defined as:

$$CM_\varnothing = \max_{t \in \varnothing}(CM_t * F(\beta_t))$$ (3)

where $F(\beta_t)$ is a squashing function for penalizing those CM_t that have β_t larger than the optimal mean included angle threshold given by (Zhu et al., 2020), i.e., $45°$,
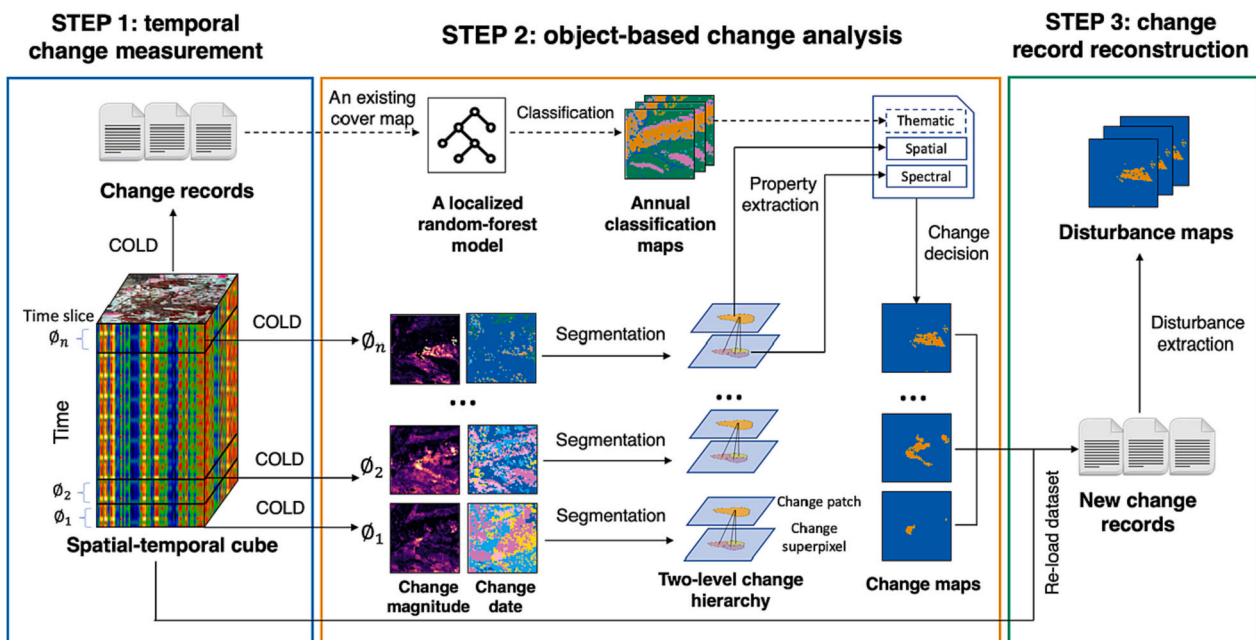

Fig. 3. The three-component workflow of OB-COLD. COLD: COntinuous monitoring of Land Disturbance; OB: Object-Based.

$$F(IA_t) = \begin{cases} 1, \beta_t < 45^\circ \\ \dfrac{90 - IA_t}{45}, 45^\circ \leq \beta_t \leq 90^\circ \\ 0, \beta_t > 90^\circ \end{cases} \tag{4}$$

Besides, the ordinal date associated with each $CM_\varnothing$ (i.e., change date) is saved to the disk during this procedure as well, which will be an essential component for the follow-up segmentation procedure as well as the new break date retrieval. It is noteworthy that the OB-COLD also looks for change magnitudes and dates in a look-backward manner during the process of detecting the start of a temporal segment after the initialization stage is determined (see Fig. 4). The look-backward setting could improve the identification of secondary disturbances occurring shortly after the first disturbance (see the example shown Fig. S4 of the supplementary material) which are often missed for the detection during the normal look-forward detection process due to a lack of an established time-series model.

The temporal interval of a time slice was empirically determined as the average days needed for accumulating five observations. With an assumption of 50% cloud/shadow chance (Zhu et al., 2020), five temporal observations ensure a probability of over 95% (i.e., $1 - 0.5^5 = 96.88\%$) for acquiring at least one clear observation within this interval. Landsat ARD dataset ideally has a temporal density of 8 days with two sensors, however, the overall average density since 1984 is between eight to 16 days due to single-sensor operation before 2000 as well as the Landsat 7 SLC-off issue. We chose a middle density, i.e., 12 days, and thus the day interval for a time slice was defined as 12 days * 5 observations = 60 days.

Once COLD is finished and regular-interval change measurements are generated for all pixels, OB-COLD reorganizes these per-pixel change magnitudes and dates into image-like snapshots indexed by time (see the examples of Fig. 5A and B). Given that a change patch might be broken into two consecutive snapshots due to a variety of factors such as cloud/shadow and SLC-off issues, change measurements from the earlier snapshot were used to fill "NA" values in the current change snapshot, with a goal of generating more spatially contiguous patches. Hence, the change dates in Fig. 5B also include the dates prior to the current processing time slice.

3.2. Object-based change analysis

Object-based change analysis was applied to process time-stamped change magnitude snapshots following a pipeline of segmentation, property extraction, and change decision.

3.2.1. Segmentation

This sub-step targets extracting two-level candidate change objects from each change measurement snapshot. It is practically difficult to directly extract meaningful change objects as some disturbance sites have considerable internal variability, therefore we applied an over-segmentation to generate a lower level of the object representation as change superpixels, pertaining the best boundary information. To derive change superpixels, OB-COLD first applies a gaussian filter with a kernel size $\sigma = 1$ on a change-magnitude snapshot, defines the initial seed pixels as the pixels with a change magnitude higher than $\chi^2_{0.90}(5)$, and then implements a mask-based Flood Fill segmentation (Bradski and Kaehler, 2000) to generate change superpixels. The pixel at (x, y) within the 8-connectivity neighborhood is considered to belong to the super-pixel of the seed pixel if its change magnitude ($CM_\varnothing$) and date ($CD_\varnothing$) meet the below conditions:

$$(1 - \lambda)*CM_\varnothing(x_{seed}, y_{seed}) \leq CM_\varnothing(x, y) \leq (1 + \lambda)*CM_\varnothing(x_{seed}, y_{seed}) \tag{5}$$

$$|CD_\varnothing(x, y) - CD_\varnothing(x_{seed}, y_{seed})| \langle time\ slice\ interval \tag{6}$$

λ is a factor that determines a fixed range centered at the change magnitude of seed pixel to connect neighborhood pixels; $\lambda = 0.4$ and $\lambda = 0.3$ have the same F_2 from the parameter sensitivity test (Table S1 in the supplementary), and $\lambda = 0.4$ was chosen due to its better efficiency (higher λ means less oversegments). Eq. (6) aims to exclude those pixels that have a change date interval longer than the time slice length with seed pixels, which were brought by the preprocessing of filling NA values using the earlier snapshot. Once a filling is finished, a mask will be updated by adding the newly filled pixels to speed up the processing for the next seed, until all seeds are processed. Admittedly, the Flood Fill algorithm is not a typical superpixel segmentation approach; we chose the Flood Fill because it exhibited the highest accuracy compared to the other two popular superpixel algorithms, including Simple Linear Iterative Clustering (SLIC) (Achanta et al., 2012) and watershed (Neubert and Protzel, 2014) (Table S1 in the supplementary). This might be because SLIC and watershed algorithms were originally designed for high-resolution color images which are not optimal for segmenting 30-m change snapshots.

After the Flood Fill segmentation is finished, change-patch objects at a broad spatial context are produced by merging adjacent change superpixels, with a hypothesis that adjacent pixels presenting spectral change within a short time are under the same change process regardless of their distinct inter-group change magnitudes (see the example of Fig. 5D). The two levels of change objects will be used to extract object properties. We tested detection performance under different scale strategies: 1) change superpixel only; 2) change patch only; 3) change superpixel and patch. The combination of change superpixel- and patch-
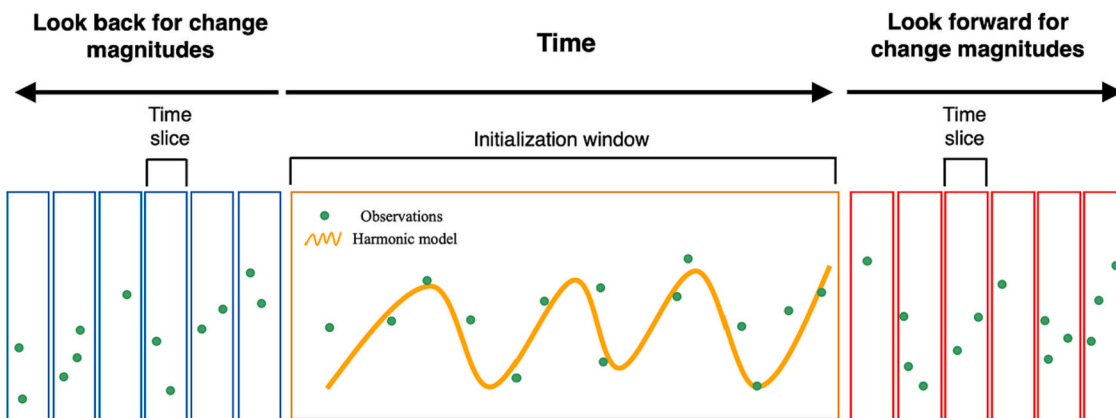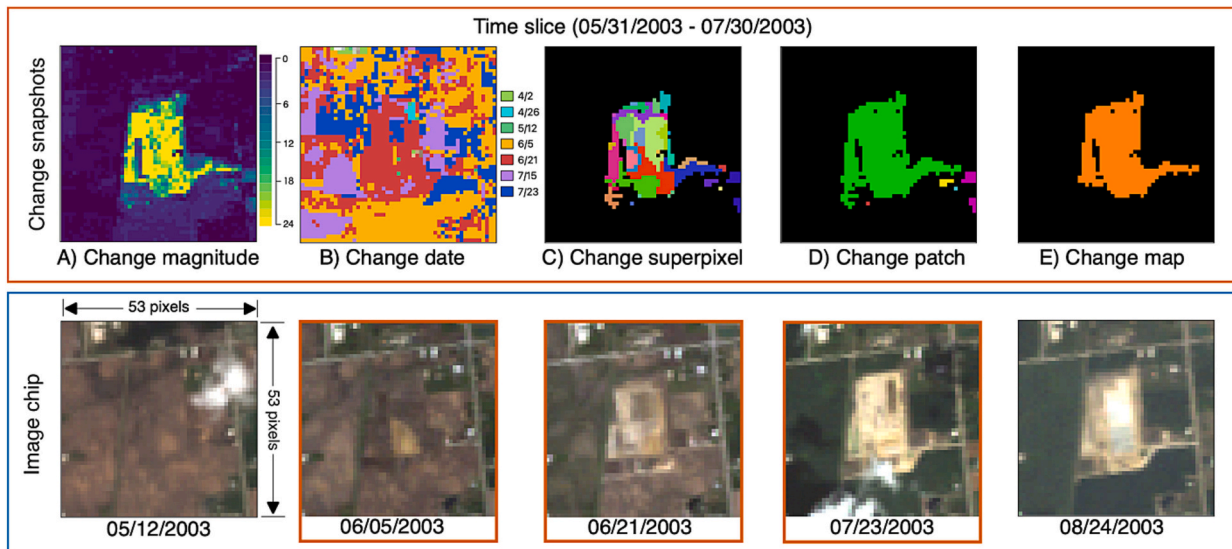

Fig. 4. Bidirectional change magnitude outputs and break identification in OB-COLD: OB-COLD saves intermediate change magnitudes from the COLD algorithm for each time slice (i.e., a regular temporal interval) in both forward and backward direction, after an initialization window is established. COLD: COntinuous monitoring of Land Disturbance; OB: Object-Based.

Fig. 5. An example site (Lat: 41.4761; Lon: −88.0881; ARD tile: H021V008) for illustrating several key steps within object-based change analysis for processing a time slice (05/31/2003–07/30/2003), coupled with its related Landsat true color composite chips (the red rectangles highlight the images collected within the time slice). A) the change magnitude snapshot and B) the change date snapshot; C) the change superpixel obtained by Flood Fill segmentation; D) the change patch generated by merging adjacent superpixels; E) the final change map through object-based change decision which could eliminate the superpixels with extremely low change magnitudes. ARD: Analysis Ready Data. (For interpretation of the references to color in this figure legend, the reader is referred to the web version of this article.)

level information showed the best F_2 (see Table S1 in the supplementary).

3.2.2. Object-level property extraction

OB-COLD assigns three object-level change properties to each candidate superpixel, relating to 1) spectral, 2) spatial, and 3) thematic features. The spectral property for a candidate superpixel is calculated as the average change magnitude of its membership pixels, indicating the overall spectral change intensity for this superpixel.

The spatial property is derived as the size of the change patch that a superpixel belongs to, which indicates the concurrent change area occurring for a time slice. Rather than the superpixel-level objects that are not meaningful geographic objects due to the over-segmentation process, patch-level objects can provide a broad view for concurrent change as evidence for a real change process against noises which usually present a random speckle pattern in both space and time.

The thematic property, as an optional object-level property for OB-COLD, requires a pre-existing land-cover map as the input (see the dash line in Fig. 2). COLD change records from the first step "temporal change measurement" define an intercept, a slope and three sets of harmonic components for each temporal segment:

$$\widehat{\rho}_{i,t} = a_{0,i} + \sum_{k=1}^{3} \left\{ a_{k,i}cos\left(\frac{2k\pi}{T}t\right) + b_{k,i}sin\left(\frac{2k\pi}{T}t\right) \right\} + c_{1,i}t \quad (7)$$

where $\widehat{\rho}_{i,t}$ is the predicted reflectance for the ith Landsat Band at Julian date t, $a_{0,i}$ is the intercept coefficient, $a_{k,i}$ and $b_{k,i}$ are kth order seasonal harmonic coefficients, $c_{1,i}$ represents the slope coefficient. To speed up processing, we selected 21 annual COLD predictors derived from COLD change records as inputted features for classification, consisting of seven overall predicted surface ($a_{0,i} + c_{1,i}t_{07-01-year}$, $i = 1, 2, …, 7th$ Bands) and 14 intra-annual coefficients of the time segment representing 1st order seasonality ($a_{1,i,year}$ and $b_{1,i,year}$, $i = 1, 2, …, 7th$ Bands). OB-COLD first builds a localized random-forest model by coupling a single-year pre-existing map with the annual COLD predictors for the year of the map. For this study, we used 2001 LCMAP land-cover product as the seed map, following the LCMAP classification system which defines eight primary land cover types (Brown et al., 2019), i.e., (1) *tree cover*, (2) *developed*, (3) *wetland*, (4) *grass/shrub*, (5) *waterbodies*,

(6) *wetland*, (7) *ice and snow*, and (8) *barren*. OB-COLD generates a total of 20,000 training sample pixels is generated following the sampling protocol provided in Zhu et al. (2016), applies the random-forest model to predict yearly land cover maps, and finally extracts the dominant pre-change cover type for each superpixel by overlaying the superpixel maps with the classified land-cover map at one year prior to its time slice ($\varnothing$),

3.2.3. Object-based change decision

To a superpixel k at a time slice $\varnothing$, the general change decision function that adjusts the object-level change magnitude by the object size is denoted as:

$$\overline{CMag}_{\varnothing,k}*scale\_factor > \chi^2_P(5) \quad (8)$$

where

$$scale\_factor = 0.95 + \left(log_{10}N_{\varnothing,k}\right)*S \quad (9)$$

$\overline{CMag}_{\varnothing,k}$ is the average change magnitude of a change superpixel. The *scale factor* is a function of the object size of its associated patch size ($N_{\varnothing,k}$, unit: pixel number). The intercept "0.95" indicates that OB-COLD only decreases the average change magnitude for the single-pixel change ($N_{\varnothing,k} = 1$) by 5%, which ensures a good performance in a heterogeneous environment where a change entity is small-sized and even smaller than Landsat pixel resolution (i.e., L-resolution). The larger change patch leads to a higher *scale factor*, hence a lower average change magnitude is needed to hit the change threshold. P and S are two key OB-COLD parameters requiring careful calibration. P determines the chi-square change threshold $\chi^2_P(5)$ (OB-COLD and COLD both use five spectral bands for calculating change magnitudes, so the degree of freedom is 5). S is a size factor that controls the weight of change patch size ($N_{\varnothing,i}$) in the decision function: when $S = 0$, only the average change magnitude is considered; a larger S yields more weights to the concurrent change area in the decision function.

This study will examine OB-COLD under two parameterization modes: the unimodal and the bimodal OB-COLD. The unimodel OB-COLD is implemented in the absence of an existing land-cover map, which applies a single set of model parameters (P, S) to all superpixels. Our grid-searching parameter test shows that the parameter set ($P =$

0.95, $S = 0$) is optimal under the unimodel situation given by its best F_2 score (Fig. S5 in the supplementary).

The bimodel OB-COLD (the default option) additionally requires a seed cover map for generating object-level thematic properties to guide applying different model parameter specifications. The two-strata land cover system ("fluctuated" vs "stable") was designed to achieve a balance between adequate per-stratum sample number and acceptable model specificity based upon Disturbance-to-Noise Ratio (DNR). DNR is defined as the ratio of the disturbance superpixels confirmed by the reference sample plots to the noisy superpixels (i.e., superpixels in those no-disturbance years). Noisy superpixels (or commission error objects) are often associated with regional change processes that belong to natural variabilities, such as climate variability, and ideally, present lower change magnitudes or smaller change patches in their attribute scatter plot. The fluctuation model is designed for the superpixels whose major pre-change categories have relatively low DNR: *cropland*, *grass/shrub*, *water*, *ice/snow*, and *barren* (Fig. 6D-E); the lower DNR indicates a higher proportion of noisy superpixels and therefore higher spectral fluctuation, suggesting a conservative model parameterization is necessitated for keeping a low commission error rate. On the other hand, the stable model is applied to identify disturbances occurring on the rest three cover types, i.e., *tree cover*, *developed*, and *wetland* (Fig. 6A-C), which has been also echoed by the past studies in forest regions (Ye et al., 2021b) or in wetland areas (Yang et al., 2022), suggesting a more sensitive change parameterization for these cover types.

Under the bimodel OB-COLD, for a superpixel object k in a time slice $\varnothing$ with its known pre-change category $LC_{\varnothing, k}$, OB-COLD identifies it as the change superpixel when:

$$\overline{CMag}_{\varnothing,i} * \left(0.95 + log_{10}N_{\varnothing,k} * S_s\right) \rangle \chi^2_{P_s}(5), \text{ if } LC_{\varnothing,k} \, \epsilon \text{ stable stratum} \tag{10}$$

$$\overline{CMag}_{\varnothing,i} * \left(0.95 + log_{10}N_{\varnothing,k} * S_f\right) \rangle \chi^2_{P_f}(5), \text{ if } LC_{\varnothing,k} \, \epsilon \text{ fluctuated stratum} \tag{11}$$

where (P_s, S_s) and (P_f, S_f) are the two parameter sets respectively for the stable and fluctuated models. To obtain the best parameter set for each model, we separated our calibration change sample plots into these two strata based on their pre-change categories predicted from the random-forest model (Section 3.2.2) and performed a grid-searching parameter test for each group. The grid-searching results (Fig. S5 in the supplementary) suggested the parameter set ($P_s = 0.95$, $S_s = 0.1$) was the best for the stable model, while ($P_f = 0.99$, $S_f = 0.05$) was the optimal for the fluctuated model due to its highest F_2 score.

3.3. Change records reconstruction and disturbance extraction

For the final step, OB-COLD generates new change records that have a consistent temporal variable set with the standard COLD (Zhu et al., 2020). OB-COLD first produces new breaks at a per-pixel level by linking resultant change maps from the second step with change date snapshots, and then recursively selects the breaks that have a day interval of at least 365 days with the last break, concerning that each temporal segment should have at least one-year interval for an efficient model fitting. As followed, a two-step protocol is applied to eliminate outliers: 1) Tmask (Zhu et al., 2019) and 2) non-consecutive outlier removal with a change-probability threshold of 0.99999 based on LASSO (Least Absolute Shrinkage and Selection Operator) model fitting. An 8-coefficient LASSO regression is built using the remaining observations to produce the final harmonic coefficients for each temporal segment.

The disturbance extraction in OB-COLD follows the same physical-rule-based approach described in Zhu et al. (2020). Given that OB-COLD additionally searches breaks in the looking-back procedure and may cause commission errors, OB-COLD introduces the second non-disturbance break type called "flipping break" besides regrowth-related breaks. Flipping breaks represent a type of break linked to the end of a disturbance process, which has an opposite spectral change direction from the previous disturbance. More details on flipping breaks
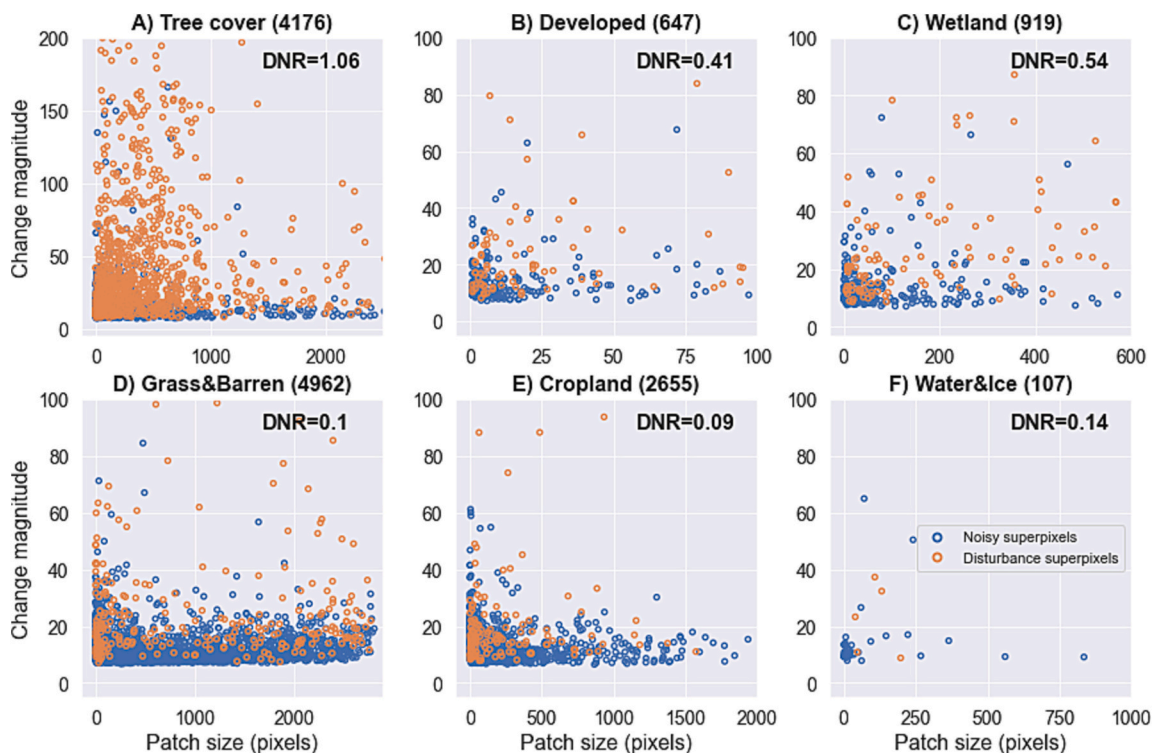
Fig. 6. Object-based attribute scatter plot and per-category Disturbance-to-Noise Ratio (DNR) based on calibration sample plots. Disturbance superpixels are those superpixels that intersect the pixel location of a reference sample and coincide with its disturbance year (correct objects), while noisy superpixels are those superpixels that intersect the sample pixel locations but occur in the no-disturbance years (commission error objects). DNR is the ratio of disturbance superpixel number to noisy superpixel number. The number in the parathesis within each sub-title indicates the total number of candidate change superpixels.

will be given in Section S2 in the supplementary material.

The COLD algorithm was written in the C language wrapped with Python API, and other components for OB-COLD were written in python; the open-source package is freely downloadable from https://github.com/GERSL/pycold.

4. Results

4.1. Quantitative assessment

The quantitative evaluation based on 2880 reference plots (Fig. 7) illustrates that the bimodel OB-COLD achieved the best F_1 (0.666) and F_2 accuracy (0.724). While its UA was similar to the COLD with the default change probability (COLD–t99) (58.7% vs. 57.8%), the bimodel OB-COLD yielded a significantly higher PA than the default COLD by 16.3% (76.9% vs. 60.6%), indicating that the primary enhancement of the bimodel OB-COLD was at reducing omission errors compared to the default COLD. Without considering pre-change cover types, the unimodel OB-COLD showed similar PAs with the bimodel (75.7% vs. 76.9%), however, at an expense of a much lower UA (46.5% vs 58.7%). As both were calibrated under F_2 objective, the unimodel OB-COLD achieved 12.2% F_2 increase compared to COLD – 95, indicating that the object-based components other than thematic components, such as segmentation procedure and object-level change decision, also greatly contribute to the accuracy improvement. The default COLD exhibited the best balance on UA and PA because it was the only approach that was calibrated based on F_1, though its F_1 was still lower than the binary OB-COLD. The COLD under the best F_2, i.e., COLD–t95, had the lowest F_1 and F_2 partly due to its extremely high commission errors (UA = 31.5%).

Disturbance detection accuracies on the individual cover type (Fig. 8) shows a large performance variation among different pre-change land status. Disturbance detection on *tree cover* (mostly relating to forest disturbances) presented the highest performance among all cover types, with relatively balanced UA and PA: the binary OB-COLD achieved >80% on both PA and UA. The types *cropland* and *grass & barren* generally showed the lowest detection performance because of their high disturbance commissions (no approaches could achieve >50% UA). *Water/ice* and *wetland* presented high PA (~80%) and moderate UA (~60%) (except COLD-t99 on *wetland*, PA = 61.4% and UA = 77.3%). For cross-approach comparison, the bimodel OB-COLD obtained the highest PA for *developed* (68.0%), *tree cover* (82.3%), *water/ice* (88.2%), and *wetland* (88.0%), while the unimodel OB-COLD achieved the highest for the rest two (*cropland*: 78.1%; *grass & barren*: 75.7%). COLD–t99 had the highest UA for most cover types (*developed*: 60.3%; *cropland*: 44.1%; *grass & barren*: 43.8%; *tree cover*: 86.7%; *wetland*: 77.3%), except for *water/ice* (the bimodal OB-COLD: 65.2%).

4.2. Qualitative assessment

The qualitative assessment shows that the default COLD approach (COLD–t99) presented under-detection for beetle outbreak, forest harvest, construction, and cropland conversion (see the example regions Fig. 9A, D, E, and G). COLD-t99 missed the detection for some pixels of the newly built solar panel site possibly because the transition from bare land to solar panels did not always present significant spectral change from their temporal profile, while the OBIA procedure in OB-COLD enabled the capture of a more complete geometry for the new solar panel site as it considers spatially concurrent change. The COLD approach under the F_2 objective (COLD–t95) presented more commission errors and salt-and-pepper noise for semiarid regions (Fig. 9F, H), and exhibited some omission errors/partial detection for wetland condition change induced by the Irma hurricane (Fig. 9C). Compared to the pixel-based approach, the unimodel and the bimodel OB-COLD generally produced more complete disturbance patch geometry with fewer omission errors. The bimodel OB-COLD performed better than the unimodel for the subtle disturbances such as beetle outbreak (see Fig. 9 B).

4.3. Detection rates by disturbance agents

The detection rates (i.e., PA) were also evaluated against six primary disturbance agents (Fig. 10). Generally, *harvest* reached higher accuracies (COLD-t95, unimodel, the bimodel OB-COLD had over 80% PA), while a lower detection rate was shown for *fire* and *stress* (all approach obtained <70% PA) possibly due to their relatively higher proportion of subtle-change cases (such as understory fire and insect disturbances). For cross-approach comparison, the default COLD (COLD–t99) exhibited the lowest PA because the default COLD was calibrated for a balanced accuracy. The unimodel and the bimodel OB-COLD presented similar PAs (the largest difference is 3.4% in *stress*), but higher PAs than the pixel-based approaches (COLD–t95 and COLD–t99) at all agents, particularly for the *stress* category where the OB-COLD achieved 19.1% accuracy gain compared to the default COLD approach.

5. Discussion

5.1. Novelty of OB-COLD

A traditional way of introducing OBIA into the time-series-based approach is postprocessing pixel-based detection results by connecting spatially and temporally adjacent break pixels into change-process objects (Hermosilla et al., 2015; Kennedy et al., 2015; Qiu et al., 2022), which we called "objectifying detection". This post-processing step for labeling objects is performed after the detection is finished, and rarely
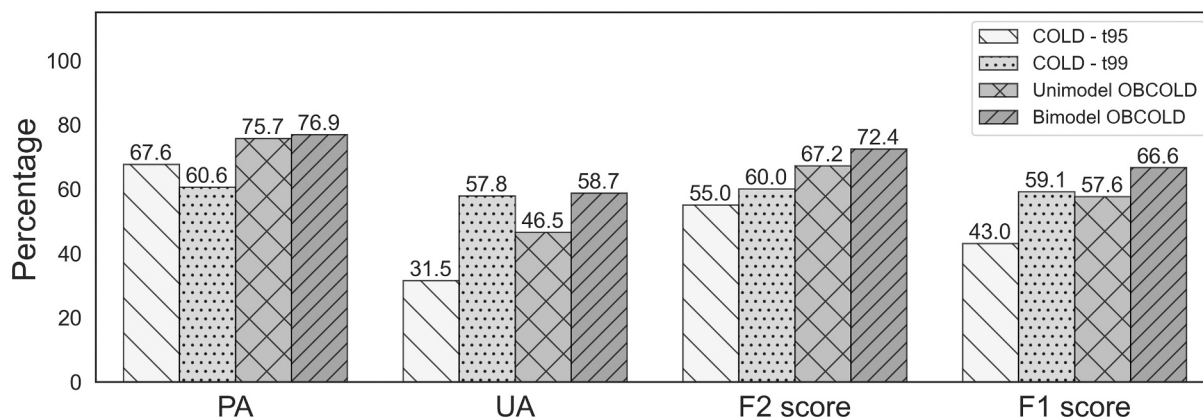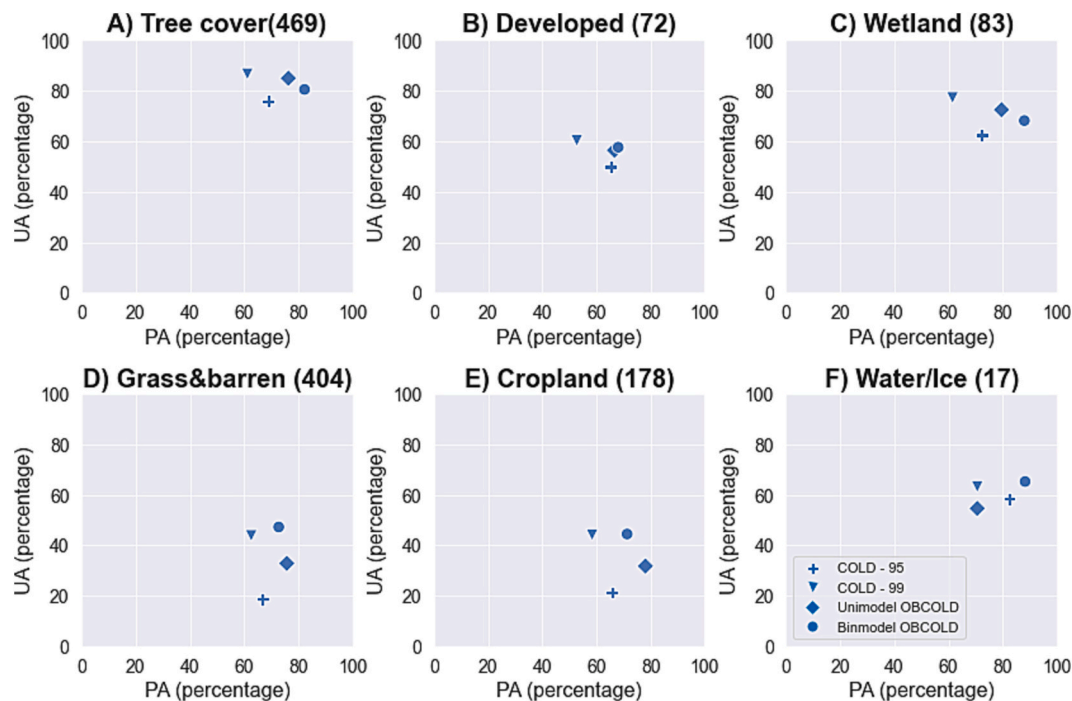

Fig. 7. Performance comparison among the pixel-based COLD algorithm under the threshold of 95% change probability (COLD-t95), the COLD algorithm with 99% change probability (COLD-t99), the unimodel OB-COLD, and the bimodel OB-COLD. COLD: COntinuous monitoring of Land Disturbance; OB: Object-Based.

Fig. 8. Producer's (PA) and user's accuracy (UA) for six pre-change land cover categories. The number in the parathesis within each sub-title indicates the change case number. The cover types were acquired by the annual land cover maps from the bimodel OB-COLD procedure. Note that COLD–95 and unimodel OB-COLD achieved identical PA and UA in F) Water/Ice so that their scatter dots were overlapped. COLD: COntinuous monitoring of Land Disturbance; OB: Object-Based.

alters the general detected region, so the accuracy of the resultant map is mostly contingent on the upstream pixel-based temporal analysis. Differently, OBIA/spatial information is employed as the key component of OB-COLD to delineate and identify disturbance regions during the detection process (hereafter named "detecting objects"). The spatial information was exhaustively analyzed in OB-COLD mainly by two steps: 1) segmenting a layer of soft change measurement from a temporal domain (i.e., change magnitude) to generate potential disturbance patch boundaries, ensuring the geometric completeness of detected patches regardless of the heterogeneity of within-patch spectral change; 2) leveraging the spatial (e.g., patch size) and the thematic object-level features (e.g., pre-change cover types) to discriminate disturbance signals from a variety of data noise and climate-induced ephemeral change. As a result, OB-COLD could possibly result in a very dissimilar disturbance map with the "objectifying detection" approach, which is exemplified by an insect-affected site shown in Fig. 11: the disturbance patches derived from OB-COLD (Fig. 11C) presented a better spatial pattern for capturing spectral changes in Fig. 11A, while the COLD results (Fig. 11B) missed some parts of the insect-affected region where the time-series profile showed an obvious window of decreasing NIR (Fig. 11E), even though the same model parameterization (change probability = 0.95) was used for both. The accuracy improvement could be also substantiated by our quantitative assessment which showed the PA of COLD-t95 was lower than that of the two OB-COLD approaches by at least 10%.

Of particular note is that object-level thematic information greatly contributes to accuracy improvement by enabling multiple cover-specific model parameterizations to be applied for generic land disturbance mapping. Compared to the unimodel OB-COLD, the bimodel OB-COLD significantly enhanced UA by 10.9% (Fig. 7). Specifically, the bimodel OB-COLD had lower disturbance over-detection for *cropland* and *barren/grass* cover types (see Fig. 8) because a more conservative parameter set for the fluctuated group was applied to these two cover types. Thematic information has been widely used as a cover mask layer to guide cover-specific disturbance detection in previous studies (Tang et al., 2019; Yang et al., 2022; Ye et al., 2021b). Assuming that the cover

type is static, most of these studies did not deal with new land covers emerging outside the mask layer. By generating and applying annual cover maps from a seed map, OB-COLD provides an easy-to-use framework for incorporating dynamic thematic information for mapping full-category or cover-specific disturbances. OB-COLD applies a robust approach based on a pixel-level majority vote to determine the thematic property for a change superpixel, which compensates for classification accuracy degradation brought by a lack of accessory datasets compared to LCMAP's CCDC implementation (Zhu et al., 2016). In practice, OB-COLD can be implemented under an unimodel, bimodel or *n*-modal setting ($n \leq$ the total number of cover categories). Our python package provides an interface for allowing users to define a customized *n*-modal system: finer model stratification will enhance the overall accuracy, and as a trade-off, requires a more sophisticated calibration for increased cover-specific parameter sets (P, S).

Lastly, OB-COLD provides a novel computationally scalable framework for approaching the grand challenge of large-scale spatiotemporal complexity: the steps of "temporal change measurement" and "change record construction" can be paralleled at the per-pixel level, and the step of "object-based change analysis" is performed on an image-based parallelization. Compared to the direct 3-D segmentation in a space-time cube that is popular in video processing (e.g., Moscheni et al., 1998), the "time-space-time" workflow has better scalability, because each parallelization unit in each step is completely independent without communications overhead between CPUs. Our efficiency tests show that the binary OB-COLD costs 1.62 times the computing hours than the original COLD (see Section S4 of the supplementary material). For the operational stage, the bimodal OB-COLD can use existing annual land cover products such as LCMAP land cover products (Xian et al., 2022) to save time for generating annual cover maps, which would result in the same computing time as the unimodal OB-COLD (only 1.37 times than the original COLD).

To summarize, OB-COLD innovates the traditional pixel-based time series analysis and other spatiotemporal change detection algorithms mainly from three perspectives: 1) fully integrating OBIA into the change-detection process rather than object labeling; 2) incorporating
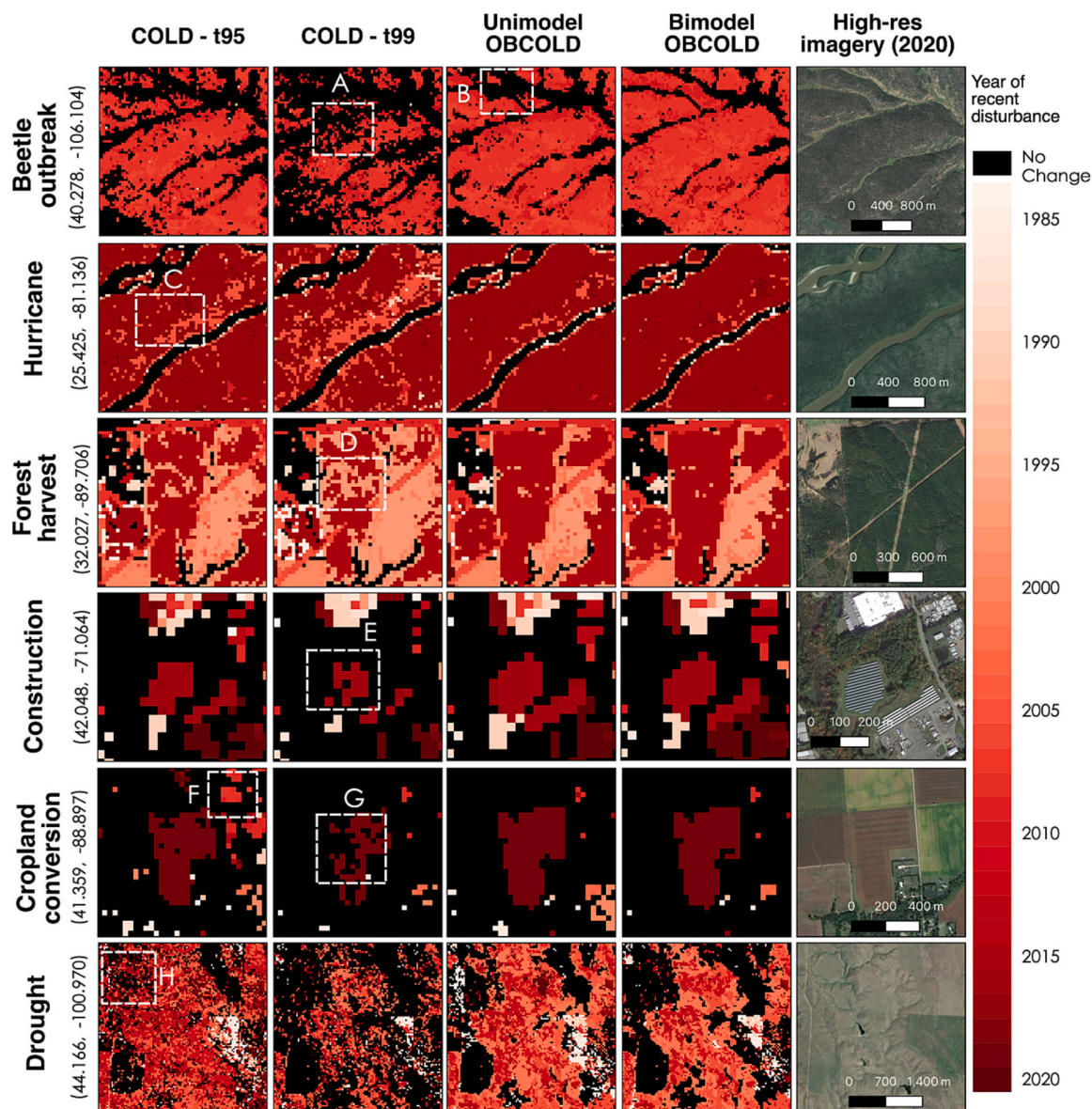
Fig. 9. Map comparison of the default COLD (COLD-t95), the COLD under the F_2 objective (COLD-t99), the unimodel OB-COLD, and the bimodel OB-COLD from the pilot Landsat ARD tiles for this study. The site locations: beetle outbreak – Rocky Colorado (h011v009); hurricane – South Florida (h027v019); forest management – Mississippi River Lowlands (h021v015); construction – New England (h030v006); agricultural practice – Corn Belt Plain (h021v008); drought– Western Great Plains (h014v006). COLD: COntinuous monitoring of Land Disturbance; OB: Object-Based; ARD: Analysis Ready Data.

thematic information; 3) enabling a computationally scalable framework to address spatiotemporal data complexity. On recognizing "land change" as multiscale objects and examining their change properties from a time-series dataset, OB-COLD is essentially different from the past time-series studies which segmented static landscape objects as analytic objects (Hughes et al., 2017; Yin et al., 2018) and various object-based change detection techniques based on an image pair (e.g., Chen et al., 2012; Im et al., 2008; Liu et al., 2021; Wan et al., 2019; Zheng et al., 2021). As a spatiotemporal algorithm that makes exhaustive use of spatial information for generic disturbance mapping, OB-COLD distinguished itself from other CCDC-like improvements such as temporal segment refinement (Bullock et al., 2020a) and spectral unmixing integration (Bullock et al., 2020b; Chen et al., 2021), which investigates spectral changes only from temporal domain and mainly set focus on forest disturbances.

5.2. Limitation and future work

Generally, the accuracies reported in this study were lower than the previous study targeting generic land disturbance (UA and PA > 70%, Zhu et al., 2019), which was primarily due to two reasons. First, the validation in Zhu et al. (2019) was based on Cohen's dataset generated from a forest-oriented sampling strategy, while forest cover has the highest disturbance detection accuracy (see Fig. 8D). The use of a forest-oriented validation set would result in higher accuracy than using a purely random sampling dataset. Second, we incorporated the recent updates on the COLD algorithm including a new single-path strategy: for the overlapped region between two paths, only observations from the path with the smaller view zenith angle (Qiu et al., 2022) remained as the algorithm inputs. This strategy increased consistencies among wall-to-wall disturbance mapping, but as a trade-off, the decreased data density negatively impacted detection accuracies, particularly for short-interval disturbances such as gypsy moth (Zhu et al., 2022). Despite the overall performance improvement, the binary OB-COLD still only has
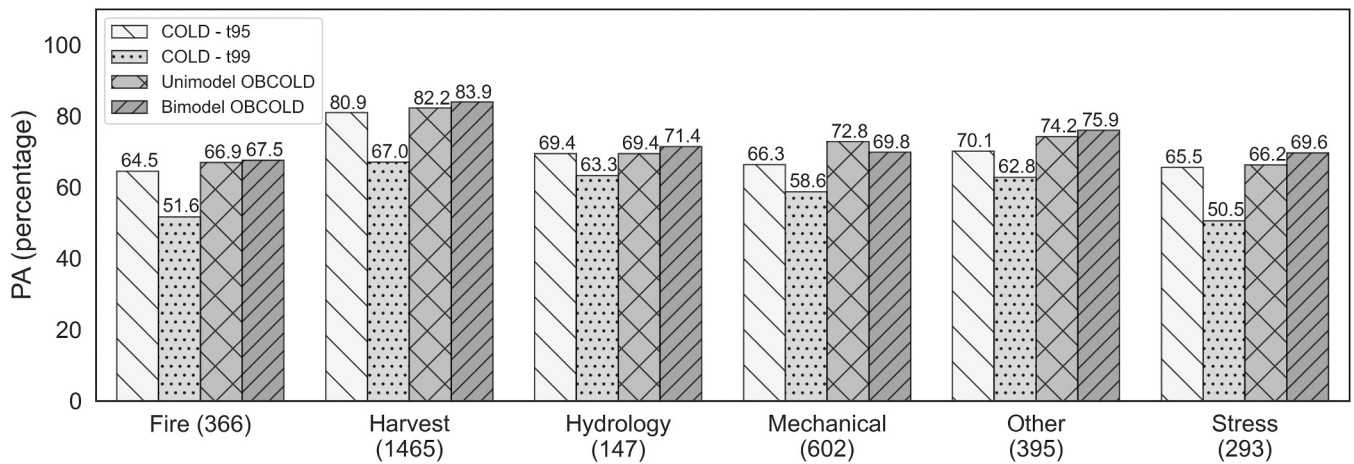
Fig. 10. Agent-specific producer accuracies based upon an assemblage of calibration and evaluation set. Note that we reclassed some categories due to inconsistencies of agent systems between Cohen's and LCMAP reference datasets: for LCMAP reference datasets, *spectral decline* and *structural decline* were combined into the *stress* category; for Cohen's reference datasets, *wind* was merged to *other* due to its small sample number (only 11 cases). LCMAP: Land Change Monitoring, Assessment, and Projection.
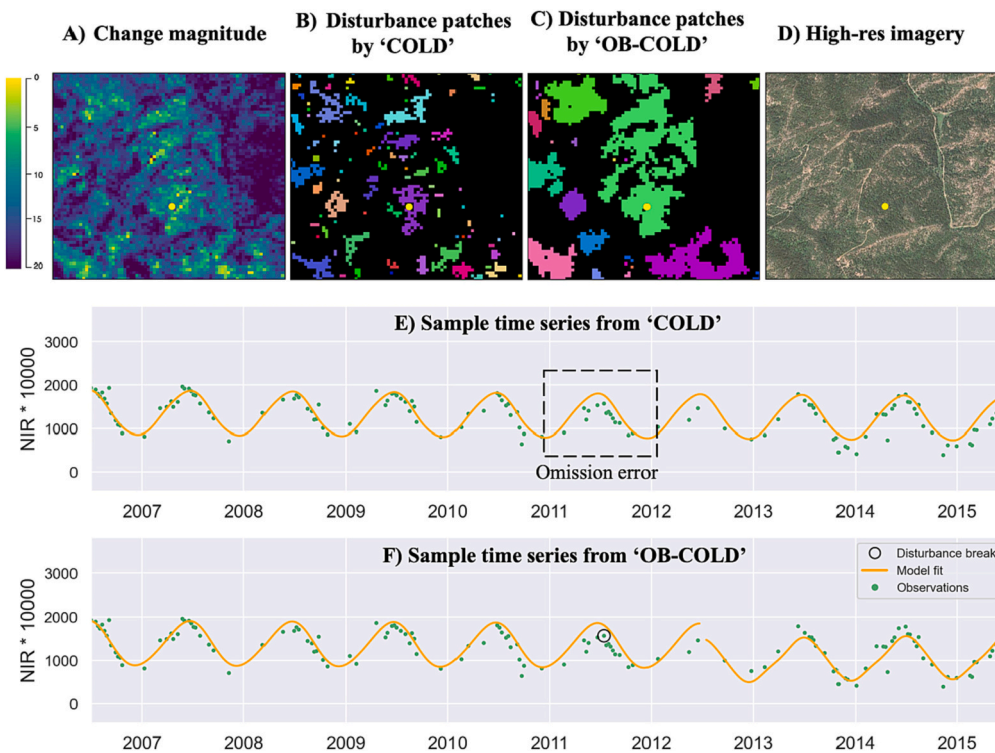
Fig. 11. A sample pixel affected by western spruce budworm (indicated by aerial surveying dataset) from the center Washington (Lat: 47.3068; Lon: −120.6689; Cascades Plateau - H004V002) for exemplifying "objectifying detection" vs "detecting objects". A) depicts a spatial pattern of contiguous increased change magnitudes induced by spruce infestation from a change magnitude snapshot (04/22/2011–06/21/2011); B) labels connected pixels of a yearly COLD disturbance map (the year of 2011, 0.95 change probability) into multiple disturbance patches (the colors represent different patches), i.e., "objectifying detection"; C) shows disturbance patch map generated from the yearly binary OB-COLD disturbance map (the year of 2011, the colors represent different patches); E) and F) exemplifies the time-series profile showing that "objectifying detection" missed some insect-affected regions where the time series shows an obvious window of decreasing NIR. COLD: COntinuous monitoring of Land Disturbance; OB: Object-Based.

58.7% UA, meaning a high level of over-detection. This is partly because we intentionally calibrated a biased model by F_2, which put less weight on commission than omission errors. Commission errors mainly occur on the cover types *cropland* and *grass/barren*, accounting for 73% of the total commissions. The over-detections were mainly attributed to climate variability and intra-annual variation of agricultural-practice timing which often leads to a large-area spatial pattern of ephemeral spectral reflectance change. Such change processes were excluded from our disturbance definition, following the most common disturbance detection protocol (Pengra et al., 2020; Zhu et al., 2019). But agricultural practices and climate variability might be of interest to other domain-specific studies (e.g., Huete, 2016; Seddon et al., 2016), and could be potentially separated out by causal agent classification techniques, such as in Zhang et al. (2022).

Different from traditional change detection based on two time points, satellite time series provides a long span of land surface dynamic history which uniquely allows for an examination of land change from multiple spatiotemporal scales. In OB-COLD, a fine temporal grain (i.e., a two-month interval for deriving objects) is chosen for the detection purpose so that we can accurately capture the change date as close to its emergence date. The temporal interval for generating change objects could be adjusted as needed by the monitoring tasks or based on the temporal resolution of the original dataset, laying a solid foundation toward near real-time monitoring adaption at a daily or weekly temporal scale in future. On the other hand, a broad temporal scale might be preferable for the downstream disturbance characterization, especially for those long-term change processes such as forest degradation (Meddens and Hicke, 2014) and urbanization (Taubenböck et al., 2012).

While disturbance characterization is beyond the scope of this study, the accurate delineation of change superpixel and patches provide a pre-requisite for generating high-quality change-process objects, which could be further used for disturbance characterization. The future study will be directed to establish a graph model that connects those spatially and temporally adjacent change patches identified by OB-COLD, similar as Wu et al. (2021) did. Compared to post-processing annual disturbance detection maps, such graph models could remove the annual bounds for defining a long-term change process and open a door for a plurality of GIS-like spatiotemporal analysis and database techniques, revolutionizing current disturbance process analytic tools and database management.

OB-COLD could be easily adapted for other Landsat-like time series datasets, such as 10-m Sentinel-2 or Harmonized Landsat Sentinel-2 (HLS), which has the potential for further enhancing the mapping capability. For example, the Sentinel-2 dataset has been reported to be superior to Landsat images for detecting small-scale disturbances such as selective logging (Lima et al., 2019); same as COLD and the LCMAP products, OB-COLD uses a peek window of six consecutive Landsat observations to identify a disturbance signal and thereby likely missed detection for those short-lived disturbances such as flash floods, which could be better detected using denser time series such as HLS dataset (Tulbure et al., 2022).

6. Conclusion

We developed a novel algorithm named "Object-Based COntinuous monitoring of Land Disturbance" (OB-COLD) for detecting land disturbances which could make better use of spatial contexts – often neglected - for the dense time-series analysis. OB-COLD is built upon the concept "concurrent change", a group of spatially adjacent pixels that are experiencing similar spectral changes within a short time interval. To extract and analyze concurrent change, OB-COLD generates change snapshots stamped by a series of time slices, groups spectrally similar change pixels into two levels of change objects, and then applies object-level change decision for each snapshot. The benefits of a such workflow are three-folded. First, OB-COLD inherits a temporal view from a well-established time-series algorithm, i.e., COLD, which measures the spectral changes relative to the historic natural variability and applies a peek window of consecutive observations for robust change magnitude calculation. Second, change magnitude snapshots, as a soft measurement of concurrent change, are an effective proxy for spectral change induced by a single change process, facilitating a spatial examination of change regions. Lastly, object-level properties introduce new insights for change detection and enhance detection accuracy, particularly for subtle change processes: the change patch size reflects concurrent change extent from a broad spatial context, as a strong indicator for real change processes against data noises; the incorporation of object-level thematic information enhances model specificity by applying cover-specific model parameterizations. Compared to the default COLD algorithm, the new algorithm improves land disturbance detection accuracies by significantly increasing PA (+16%) without degraded UA. Despite ~40% of commission errors, most commission errors (73%) are attributed to agricultural practices and climate variability. The proposed algorithm owns high algorithmic transparency and computationally scalability for large-scale datasets with advanced computing resources, holding great potential as the base detection algorithm for the next generation of land disturbance products.

CRediT authorship contribution statement

Su Ye: Conceptualization, Methodology, Software, Writing – original draft. **Zhe Zhu:** Conceptualization, Writing – review & editing. **Guofeng Cao:** Writing – review & editing.

Appendix A. Supplementary data

Supplementary data to this article can be found online at https://doi.org/10.1016/j.rse.2023.113462.

References

Achanta, R., Shaji, A., Smith, K., Lucchi, A., Fua, P., Süsstrunk, S., 2012. SLIC superpixels compared to state-of-the-art superpixel methods. IEEE Trans. Pattern Anal. Mach. Intell. 34, 2274–2282.

Baeza-Yates, R., Ribeiro-Neto, B., 1999. Modern information retrieval. ACM press, New York.

Baumann, M., Ozdogan, M., Wolter, P.T., Krylov, A., Vladimirova, N., Radeloff, V.C., 2014. Landsat remote sensing of forest windfall disturbance. Remote Sens. Environ. 143, 171–179.

Belgiu, M., Csillik, O., 2018. Sentinel-2 cropland mapping using pixel-based and object-based time-weighted dynamic time warping analysis. Remote Sens. Environ. https://doi.org/10.1016/j.rse.2017.10.005.

Bian, L., 2007. Object-oriented representation of environmental phenomena: is everything best represented as an object? Ann. Assoc. Am. Geogr. https://doi.org/10.1111/j.1467-8306.2007.00535.x.

Blaschke, T., 2010. Object based image analysis for remote sensing. ISPRS J. Photogramm. Remote Sens. https://doi.org/10.1016/j.isprsjprs.2009.06.004.

Blaschke, T., Hay, G.J., Kelly, M., Lang, S., Hofmann, P., Addink, E., Feitosa, R.Q., Van der Meer, F., Van der Werff, H., Van Coillie, F., 2014. Geographic object-based image analysis–towards a new paradigm. ISPRS J. Photogramm. Remote Sens. 87, 180–191.

Bradski, G., Kaehler, A., 2000. OpenCV. Dr. Dobb's J. Softw. Tools 3, 120.

Brown, J.F., Tollerud, H.J., Barber, C.P., Zhou, Q., Dwyer, J.L., Vogelmann, J.E., Loveland, T.R., Woodcock, C.E., Stehman, S.V., Zhu, Z., Pengra, B.W., Smith, K., Horton, J.A., Xian, G., Auch, R.F., Sohl, T.L., Sayler, K.L., Gallant, A.L., Zelenak, D., Reker, R.R., Rover, J., 2019. Lessons learned implementing an operational continuous United States national land change monitoring capability: the land change monitoring, assessment, and projection (LCMAP) approach. Remote Sens. Environ. https://doi.org/10.1016/j.rse.2019.111356.

Carey, R.O., Migliaccio, K.W., Li, Y., Schaffer, B., Kiker, G.A., Brown, M.T., 2011. Land use disturbance indicators and water quality variability in the Biscayne Bay Watershed, Florida. Ecol. Indic. 11, 1093–1104.

Chen, G., Hay, G.J., Carvalho, L.M.T., Wulder, M.A., 2012. Object-based change detection. Int. J. Remote Sens. 33, 4434–4457.

Cleve, C., Kelly, M., Kearns, F.R., Moritz, M., 2008. Classification of the wildland–urban interface: a comparison of pixel-and object-based classifications using high-resolution aerial photography. Comput. Environ. Urban. Syst. 32, 317–326.

Cohen, W.B., Healey, S.P., Yang, Z., Stehman, S.V., Brewer, C.K., Brooks, E.B., Gorelick, N., Huang, C., Hughes, M.J., Kennedy, R.E., 2017. How similar are Forest disturbance maps derived from different landsat time series Algorithms? For. Trees Livelihoods 8, 98.

Cohen, W.B., Yang, Z., Healey, S.P., Kennedy, R.E., Gorelick, N., 2018. A LandTrendr multispectral ensemble for forest disturbance detection. Remote Sens. Environ. 205, 131–140.

Cohen, W.B., Yang, Z., Kennedy, R., 2010. Detecting trends in forest disturbance and recovery using yearly landsat time series: 2. TimeSync—Tools for calibration and validation. Remote Sens. Environ. 114, 2911–2924.

Cohen, W.B., Yang, Z., Stehman, S.V., Schroeder, T.A., Bell, D.M., Masek, J.G., Huang, C., Meigs, G.W., 2016. Forest disturbance across the conterminous United States from 1985–2012: the emerging dominance of forest decline. For. Ecol. Manag. 360, 242–252. https://doi.org/10.1016/j.foreco.2015.10.042.

Coops, N.C., Shang, C., Wulder, M.A., White, J.C., Hermosilla, T., 2020. Change in forest condition: characterizing non-stand replacing disturbances using time series satellite imagery. For. Ecol. Manag. https://doi.org/10.1016/j.foreco.2020.118370.

Csillik, O., 2017. Fast segmentation and classification of very high resolution remote sensing data using SLIC superpixels. Remote Sens. 9, 243.

Dale, V.H., Joyce, L.A., McNulty, S., Neilson, R.P., Ayres, M.P., Flannigan, M.D., Hanson, P.J., Irland, L.C., Lugo, A.E., Peterson, C.J., 2001. Climate change and forest disturbances: climate change can affect forests by altering the frequency, intensity, duration, and timing of fire, drought, introduced species, insect and pathogen outbreaks, hurricanes, windstorms, ice storms, or landslides. Bioscience 51, 723–734.

Danneyrolles, V., Dupuis, S., Fortin, G., Leroyer, M., de Römer, A., Terrail, R., Vellend, M., Boucher, Y., Laflamme, J., Bergeron, Y., Arseneault, D., 2019. Stronger influence of anthropogenic disturbance than climate change on century-scale compositional changes in northern forests. Nat. Commun. https://doi.org/10.1038/s41467-019-09265-z.

Djerriri, K., Safia, A., Adjoudj, R., 2020. Object-based classification of Sentinel-2 imagery using compact texture unit descriptors through Google Earth Engine. In: 2020 Mediterr. Middle-East Geosci. Remote Sens. Symp. M2GARSS 2020 - Proc. https://doi.org/10.1109/M2GARSS47143.2020.9105181.

Dronova, I., Gong, P., Wang, L., Zhong, L., 2015. Mapping dynamic cover types in a large seasonally flooded wetland using extended principal component analysis and object-based classification. Remote Sens. Environ. 158, 193–206.

Duveiller, G., Defourny, P., Desclée, B., Mayaux, P., 2008. Deforestation in Central Africa: estimates at regional, national and landscape levels by advanced processing of systematically-distributed landsat extracts. Remote Sens. Environ. https://doi.org/10.1016/j.rse.2007.07.026.

Dwyer, J., Roy, D., Sauer, B., Jenkerson, C., Zhang, H., Lymburner, L., 2018. Analysis ready data: enabling analysis of the landsat archive. Remote Sens. 10 https://doi.org/10.20944/preprints201808.0029.v1.

Galbraith, S.M., Cane, J.H., Moldenke, A.R., Rivers, J.W., 2019. Salvage logging reduces wild bee diversity, but not abundance, in severely burned mixed-conifer forest. For. Ecol. Manag. 453, 117622.

Gómez, C., White, J.C., Wulder, M.A., 2011. Characterizing the state and processes of change in a dynamic forest environment using hierarchical spatio-temporal segmentation. Remote Sens. Environ. 115, 1665–1679.

Gudex-Cross, D., Pontius, J., Adams, A., 2017. Enhanced forest cover mapping using spectral unmixing and object-based classification of multi-temporal landsat imagery. Remote Sens. Environ. 196, 193–204.

Hamunyela, E., Verbesselt, J., Herold, M., 2016. Using spatial context to improve early detection of deforestation from landsat time series. Remote Sens. Environ. 172, 126–138. https://doi.org/10.1016/j.rse.2015.11.006.

Healey, S.P., Cohen, W.B., Yang, Z., Kenneth Brewer, C., Brooks, E.B., Gorelick, N., Hernandez, A.J., Huang, C., Joseph Hughes, M., Kennedy, R.E., Loveland, T.R., Moisen, G.G., Schroeder, T.A., Stehman, S.V., Vogelmann, J.E., Woodcock, C.E., Yang, L., Zhu, Z., 2018. Mapping forest change using stacked generalization: an ensemble approach. Remote Sens. Environ. 204, 717–728. https://doi.org/10.1016/j.rse.2017.09.029.

Hermosilla, T., Wulder, M.A., White, J.C., Coops, N.C., 2019. Prevalence of multiple forest disturbances and impact on vegetation regrowth from interannual landsat time series (1985–2015). Remote Sens. Environ. https://doi.org/10.1016/j.rse.2019.111403.

Hermosilla, T., Wulder, M.A., White, J.C., Coops, N.C., Hobart, G.W., 2015. Regional detection, characterization, and attribution of annual forest change from 1984 to 2012 using landsat-derived time-series metrics. Remote Sens. Environ. https://doi.org/10.1016/j.rse.2015.09.004.

Holt, A.C., Seto, E.Y.W., Rivard, T., Gong, P., 2009. Object-based detection and classification of vehicles from high-resolution aerial photography. Photogramm. Eng. Remote Sens. 75, 871–880.

Huang, C., Goward, S.N., Masek, J.G., Thomas, N., Zhu, Z., Vogelmann, J.E., 2010. An automated approach for reconstructing recent forest disturbance history using dense landsat time series stacks. Remote Sens. Environ. 114, 183–198.

Huete, A., 2016. Vegetation's responses to climate variability. Nature 531, 181–182.

Im, J., Jensen, J.R., Tullis, J.A., 2008. Object-based change detection using correlation image analysis and image segmentation. Int. J. Remote Sens. 29, 399–423.

Jobin, B., Labrecque, S., Grenier, M., Falardeau, G., 2008. Object-based classification as an alternative approach to the traditional pixel-based classification to identify potential habitat of the grasshopper sparrow. Environ. Manag. https://doi.org/10.1007/s00267-007-9031-0.

Kennedy, R.E., Yang, Z., Braaten, J., Copass, C., Antonova, N., Jordan, C., Nelson, P., 2015. Attribution of disturbance change agent from landsat time-series in support of habitat monitoring in the Puget Sound region, USA. Remote Sens. Environ. 166, 271–285.

Kennedy, R.E., Yang, Z., Cohen, W.B., 2010. Detecting trends in forest disturbance and recovery using yearly landsat time series: 1. LandTrendr—Temporal segmentation algorithms. Remote Sens. Environ. 114, 2897–2910.

Kimmins, J., 2004. Forest Ecology – A Foundation for Sustainable Forest Management and Environmental Ethics in Forestry. Prentice Hall, Up. Saddle Saddle River, New Jersey.

Laurent, V.C.E., Verhoef, W., Damm, A., Schaepman, M.E., Clevers, J.G.P.W., 2013. A bayesian object-based approach for estimating vegetation biophysical and biochemical variables from APEX at-sensor radiance data. Remote Sens. Environ. 139, 6–17.

Li, T., Zhu, Z., Wang, Z., Román, M.O., Kalb, V.L., Zhao, Y., 2022. Continuous monitoring of nighttime light changes based on daily NASA's black marble product suite. Remote Sens. Environ. 282, 113269.

Liang, L., Chen, Y., Hawbaker, T.J., Zhu, Z., Gong, P., 2014. Mapping mountain pine beetle mortality through growth trend analysis of time-series landsat data. Remote Sens. https://doi.org/10.3390/rs6065696.

Lima, T.A., Beuchle, R., Langner, A., Grecchi, R.C., Griess, V.C., Achard, F., 2019. Comparing Sentinel-2 MSI and landsat 8 OLI imagery for monitoring selective logging in the brazilian Amazon. Remote Sens. 11, 961.

Liu, T., Yang, L., Lunga, D., 2021. Change detection using deep learning approach with object-based image analysis. Remote Sens. Environ. 256, 112308.

Martínez-Ramos, M., Ortiz-Rodríguez, I.A., Piñero, D., Dirzo, R., Sarukhán, J., 2016. Anthropogenic disturbances jeopardize biodiversity conservation within tropical rainforest reserves. Proc. Natl. Acad. Sci. U. S. A. https://doi.org/10.1073/pnas.1602893113.

Meddens, A.J.H., Hicke, J.A., 2014. Spatial and temporal patterns of Landsat-based detection of tree mortality caused by a mountain pine beetle outbreak in Colorado, USA. For. Ecol. Manage. 322, 78–88.

Meng, Y., Liu, X., Wang, Z., Ding, C., Zhu, L., 2021. How can spatial structural metrics improve the accuracy of forest disturbance and recovery detection using dense landsat time series? Ecol. Indic. 132, 108336.

Moscheni, F., Bhattacharjee, S., Kunt, M., 1998. Spatio-temporal segmentation based on region merging. IEEE Trans. Pattern Anal. Mach. Intell. 20, 897–915.

Neubert, P., Protzel, P., 2014. Compact watershed and preemptive slic: On improving trade-offs of superpixel segmentation algorithms. In: 2014 22nd International Conference on Pattern Recognition. IEEE, pp. 996–1001.

Newman, E.A., 2019. Disturbance ecology in the anthropocene. Front. Ecol. Evol. 7 https://doi.org/10.3389/fevo.2019.00147.

Pasquarella, V.J., Bradley, B.A., Woodcock, C.E., 2017. Near-real-time monitoring of insect defoliation using landsat time series. Forests 8. https://doi.org/10.3390/f8080275.

Pengra, B.W., Stehman, S.V., Horton, J.A., Dockter, D.J., Schroeder, T.A., Yang, Z., Cohen, W.B., Healey, S.P., Loveland, T.R., 2020. Quality control and assessment of interpreter consistency of annual land cover reference data in an operational national monitoring program. Remote Sens. Environ. 238, 111261.

Qiu, S., Zhu, Z., Yang, X., 2022. Characterization of land disturbances based on Landsat time series. Remote Sens. Environ.

Rodman, K.C., Andrus, R.A., Veblen, T.T., Hart, S.J., 2021. Disturbance detection in landsat time series is influenced by tree mortality agent and severity, not by prior disturbance. Remote Sens. Environ. https://doi.org/10.1016/j.rse.2020.112244.

Roelfsema, C.M., Lyons, M., Kovacs, E.M., Maxwell, P., Saunders, M.I., Samper-Villarreal, J., Phinn, S.R., 2014. Multi-temporal mapping of seagrass cover, species and biomass: a semi-automated object based image analysis approach. Remote Sens. Environ. 150, 172–187.

Rogan, J., Miller, J., 2006. Integrating GIS and remotely sensed data for mapping forest disturbance and change. Underst. For. Disturb. Spat. Pattern. https://doi.org/10.1201/9781420005189.ch6.

Schug, F., Okujeni, A., Hauer, J., Hostert, P., Nielsen, J.Ø., van der Linden, S., 2018. Mapping patterns of urban development in Ouagadougou, Burkina Faso, using machine learning regression modeling with bi-seasonal landsat time series. Remote Sens. Environ. 210, 217–228.

Seddon, A.W.R., Macias-Fauria, M., Long, P.R., Benz, D., Willis, K.J., 2016. Sensitivity of global terrestrial ecosystems to climate variability. Nature 531, 229–232.

Seidl, R., Schelhaas, M.-J., Rammer, W., Verkerk, P.J., 2014. Increasing forest disturbances in Europe and their impact on carbon storage. Nat. Clim. Chang. 4, 806–810.

Seidl, R., Thom, D., Kautz, M., Martin-Benito, D., Peltoniemi, M., Vacchiano, G., Wild, J., Ascoli, D., Petr, M., Honkaniemi, J., 2017. Forest disturbances under climate change. Nat. Clim. Chang. 7, 395–402.

Senf, C., Seidl, R., 2021. Mapping the forest disturbance regimes of Europe. Nat. Sustain. 4, 63–70.

Senf, C., Seidl, R., Hostert, P., 2017. Remote sensing of forest insect disturbances: current state and future directions. Int. J. Appl. Earth Obs. Geoinf. 60, 49–60.

Solórzano, J.V., Gao, Y., 2022. Forest disturbance detection with seasonal and trend model components and machine learning algorithms. Remote Sens. 14, 803.

Stehman, S.V., Pengra, B.W., Horton, J.A., Wellington, D.F., 2021. Validation of the US geological Survey's land change monitoring, assessment and projection (LCMAP) collection 1.0 annual land cover products 1985–2017. Remote Sens. Environ. 265, 112646.

Strahler, A.H., Woodcock, C.E., Smith, J.A., 1986. On the nature of models in remote sensing. Remote Sens. Environ. 20 (2), 121–139.

Tang, X., Bullock, E.L., Olofsson, P., Estel, S., Woodcock, C.E., 2019. Near real-time monitoring of tropical forest disturbance: new algorithms and assessment framework. Remote Sens. 224, 202–218.

Taubenböck, H., Esch, T., Felbier, A., Wiesner, M., Roth, A., Dech, S., 2012. Monitoring urbanization in mega cities from space. Remote Sens. Environ. 117, 162–176.

Tulbure, M.G., Broich, M., Perin, V., Gaines, M., Ju, J., Stehman, S.V., Pavelsky, T., Masek, J.G., Yin, S., Mai, J., 2022. Can we detect more ephemeral floods with higher density harmonized landsat sentinel 2 data compared to landsat 8 alone? ISPRS J. Photogramm. Remote Sens. 185, 232–246.

Verbesselt, J., Hyndman, R., Newnham, G., Culvenor, D., 2010. Detecting trend and seasonal changes in satellite image time series. Remote Sens. Environ. 114, 106–115. https://doi.org/10.1016/j.rse.2009.08.014.

Vieira, M.A., Formaggio, A.R., Rennó, C.D., Atzberger, C., Aguiar, D.A., Mello, M.P., 2012. Object based image analysis and data mining applied to a remotely sensed landsat time-series to map sugarcane over large areas. Remote Sens. Environ. https://doi.org/10.1016/j.rse.2012.04.011.

Villarreal, M.L., Norman, L.M., Buckley, S., Wallace, C.S.A., Coe, M.A., 2016. Multi-index time series monitoring of drought and fire effects on desert grasslands. Remote Sens. Environ. 183, 186–197.

Wan, L., Xiang, Y., You, H., 2019. An object-based hierarchical compound classification method for change detection in heterogeneous optical and SAR images. IEEE Trans. Geosci. Remote Sens. 57, 9941–9959.

White, J.C., Hermosilla, T., Wulder, M.A., Coops, N.C., 2022. Mapping, validating, and interpreting spatio-temporal trends in post-disturbance forest recovery. Remote Sens. Environ. 271, 112904.

White, P.S., Pickett, S.T.A., 1985. Natural disturbance and patch dynamics: an introduction. Ecol. Nat. Disturb. Patch Dyn. https://doi.org/10.1016/b978-0-12-554520-4.50006-x.

Wu, B., Yu, B., Shu, S., Wu, Q., Zhao, Y., Wu, J., 2021. A spatiotemporal structural graph for characterizing land cover changes. Int. J. Geogr. Inf. Sci. 35, 397–425.

Xian, G.Z., Smith, K., Wellington, D., Horton, J., Zhou, Q., Li, C., Auch, R., Brown, J.F., Zhu, Z., Reker, R.R., 2022. Implementation of the CCDC algorithm to produce the LCMAP collection 1.0 annual land surface change product. Earth Syst. Sci. Data 14, 143–162.

Yang, X., Zhu, Zhe, Qiu, S., Kroeger, K.D., Zhu, Zhiliang, Covington, S., 2022. Detection and characterization of coastal tidal wetland change in the northeastern US using landsat time series. Remote Sens. Environ. 276, 113047.

Ye, S., Rogan, J., Zhu, Z., Eastman, J.R., 2021a. A near-real-time approach for monitoring forest disturbance using landsat time series: stochastic continuous change detection. Remote Sens. Environ. https://doi.org/10.1016/j.rse.2020.112167.

Ye, S., Rogan, J., Zhu, Z., Hawbaker, T.J., Hart, S.J., Andrus, R.A., Meddens, A.J.H., Hicke, J.A., Eastman, J.R., Kulakowski, D., 2021b. Detecting subtle change from dense landsat time series: case studies of mountain pine beetle and spruce beetle disturbance. Remote Sens. Environ. https://doi.org/10.1016/j.rse.2021.112560.

Yin, H., Brandão Jr., A., Buchner, J., Helmers, D., Iuliano, B.G., Kimambo, N.E., Lewińska, K.E., Razenkova, E., Rizayeva, A., Rogova, N., 2020. Monitoring cropland abandonment with landsat time series. Remote Sens. Environ. 246, 111873.

Yin, H., Prishchepov, A.V., Kuemmerle, T., Bleyhl, B., Buchner, J., Radeloff, V.C., 2018. Mapping agricultural land abandonment from spatial and temporal segmentation of landsat time series. Remote Sens. Environ. 210, 12–24.

Yuan, M., 2001. Representing complex geographic phenomena in GIS. Cartogr. Geogr. Inf. Sci. 28, 83–96.

Zhang, C., Cooper, H., Selch, D., Meng, X., Qiu, F., Myint, S.W., Roberts, C., Xie, Z., 2014. Mapping urban land cover types using object-based multiple endmember spectral mixture analysis. Remote Sens. Lett. 5, 521–529.

Zhang, C., Sargent, I., Pan, X., Li, H., Gardiner, A., Hare, J., Atkinson, P.M., 2018. An object-based convolutional neural network (OCNN) for urban land use classification. Remote Sens. Environ. 216, 57–70.

Zhang, Y., Atkinson, P.M., Ling, F., Foody, G.M., Wang, Q., Ge, Y., Li, X., Du, Y., 2021. Object-based area-to-point regression kriging for pansharpening. IEEE Trans. Geosci. Remote Sens. 59, 8599–8614.

Zhang, Y., Woodcock, C.E., Chen, S., Wang, J.A., Sulla-Menashe, D., Zuo, Z., Olofsson, P., Wang, Y., Friedl, M.A., 2022. Mapping causal agents of disturbance in boreal and arctic ecosystems of North America using time series of landsat data. Remote Sens. Environ. 272, 112935.

Zheng, Z., Zhong, Y., Wang, J., Ma, A., Zhang, L., 2021. Building damage assessment for rapid disaster response with a deep object-based semantic change detection framework: from natural disasters to man-made disasters. Remote Sens. Environ. 265, 112636.

Zhu, Z., 2017. Change detection using landsat time series: a review of frequencies, preprocessing, algorithms, and applications. ISPRS J. Photogramm. Remote Sens. 130, 370–384.

Zhu, Z., Gallant, A.L., Woodcock, C.E., Pengra, B., Olofsson, P., Loveland, T.R., Jin, S., Dahal, D., Yang, L., Auch, R.F., 2016. Optimizing selection of training and auxiliary data for operational land cover classification for the LCMAP initiative. ISPRS J. Photogramm. Remote Sens. 122, 206–221.

Zhu, Z., Qiu, S., Ye, S., 2022. Remote sensing of land change: a multifaceted perspective. Remote Sens. Environ. 282, 113266.

Zhu, Z., Woodcock, C.E., 2014a. Continuous change detection and classification of land cover using all available landsat data. Remote Sens. Environ. 144, 152–171.

Zhu, Z., Woodcock, C.E., 2014b. Automated cloud, cloud shadow, and snow detection in multitemporal landsat data: an algorithm designed specifically for monitoring land cover change. Remote Sens. Environ. 152, 217–234.

Zhu, Z., Woodcock, C.E., 2012. Object-based cloud and cloud shadow detection in landsat imagery. Remote Sens. Environ. 118, 83–94.

Zhu, Z., Zhang, J., Yang, Z., Aljaddani, A.H., Cohen, W.B., Qiu, S., Zhou, C., 2020. Continuous monitoring of land disturbance based on landsat time series. Remote Sens. Environ. https://doi.org/10.1016/j.rse.2019.03.009.

Zhu, Z., Zhang, J., Yang, Z., Aljaddani, A.H., Cohen, W.B., Qiu, S., Zhou, C., 2019. Continuous monitoring of land disturbance based on landsat time series. Remote Sens. Environ. https://doi.org/10.1016/j.rse.2019.03.009.